OXFORD UNIVERSITY PRESS | Journal of Petrology

Draft Manuscript for Review

Compositional and petrological assembly of a mush-bearing magma reservoir in Tenerife

Journal:	*Journal of Petrology*
Manuscript ID	JPET-Aug-21-0112.R2
Manuscript Type:	Original Manuscript
Date Submitted by the Author:	06-Sep-2022
Complete List of Authors:	Horn, Emma; University of Southampton School of Ocean and Earth Science, Taylor, Rex; University of Southampton School of Ocean and Earth Science Gernon, Thomas; University of Southampton School of Ocean and Earth Science Stock, Michael J; Trinity College Dublin, Department of Geology Farley, E. M. Ruth; University of Southampton School of Ocean and Earth Science
Keyword:	cumulate, geochemistry, igneous petrology, OIB, mush
Journal of Petrology now offers Virtual Collections of published papers. You may choose up to three collections from the list below. Virtual collections will increase the visibility of your work.:	Alkaline rocks < Material Themes, Oceanic Intraplate Magmatism < Province Themes

Compositional and petrological assembly of a mush-bearing magma reservoir in Tenerife

Emma L. Horn[1]*, Rex N. Taylor[1], Thomas M. Gernon[1], Michael J. Stock[2], E.M. Ruth Farley[1]
[1]School of Ocean and Earth Science, University of Southampton, Waterfront Campus, Southampton, SO14 3ZH, UK
[2]Department of Geology, Trinity College Dublin, College Green, Dublin 2, Ireland.
*Corresponding author email address: e.l.horn@soton.ac.uk

ABSTRACT

Deciphering the dynamics of sub-volcanic magmatic processes requires a detailed understanding of the compositional and textural relationships between melt and crystals. To examine these relationships, we investigated material from one of the largest caldera-forming explosive eruptions on the ocean island of Tenerife, the 312 ka Fasnia event. This eruption ejected juvenile pyroclasts of melt-bearing, partially crystalline cumulate nodules alongside phonolitic pumice and accidental lithic clasts. Nodules contain an average of 26% melt which is preserved as vesiculated and microcrystalline basanite in segregations, pathways and interstitial domains. Both the microcrystalline groundmass and crystal framework are generally unaltered as this crystal ‘mush’ remained supra-solidus until the eruption. We find no surficial or intrinsic evidence that the nodules were transported from their reservoir in a ‘carrier’ magma, and it is most likely that the mush was in situ when it was explosively fragmented and ejected during eruption. As such, the nodules preserve a record of the proportions and relationships between the crystal framework and pre-eruptive melt in an active magma mush reservoir; importantly, capturing a snapshot of the sub-volcanic system at a single point in time. We have analysed >100 of the mush nodules from the massive lithic breccia facies within the Fasnia Member of the Diego Hernández Formation. These cumulates span a diverse range of alkaline plutonic lithologies, from wehrlite and pyroxenite, through hornblende gabbros, to monzodiorite and syenite. Their textures record a range of crystallisation environments, including both crystal- and melt-rich groundmass domains, and invasion of near-solidus domains by ascending reactive melts. In addition, the cumulus phases record complex interactions between felsic and mafic magmas throughout their development, providing evidence for mush remobilization and disequilibrium. Relative homogeneity of melt compositions through the mafic and felsic lithologies testifies to melt mobility through the cumulates. Nevertheless, all melts are of different basanite-intermediate composition to the juvenile phonolitic pumice ejected during the same eruption. This observation implies that the mafic-felsic cumulate mush and the phonolite did not experience significant two-way mixing and existed as separate crustal reservoirs. . However, the Fasnia eruption simultaneously fragmented and removed material from both reservoirs, implying the mafic system was subjacent to the felsic, but they did not form a contiguous body.

KEY WORDS

alkaline magmatism; crystal mush; cumulates; mineral geochemistry; ocean island volcanism

INTRODUCTION

Detailed petrological, geochemical and geophysical studies of individual magmatic systems have shown that long-lived storage regions are dominantly composed of 'mushes'; frameworks of crystals and domains of melt-rich pockets or sills (Cashman *et al.*, 2017, Edmonds *et al.*, 2019, Sparks *et al.*, 2019, Wager *et al.*, 1960). Examination of plutonic material in the form of cumulate nodules, enclaves and xenoliths has been key to constraining the spatial extent and compositional characteristics of these mush systems, providing textural and geochemical evidence for high degrees of chemical heterogeneity, open system processes and multiple melt source depths (Bachmann & Bergantz, 2008, Cooper *et al.*, 2016, Holness *et al.*, 2019, Jackson *et al.*, 2018, Stock *et al.*, 2020). These plutonic components have advanced our understanding of melt differentiation and storage in long-lived mush reservoirs

(Cooper *et al.*, 2016, Gleeson *et al.*, 2020, Jackson *et al.*, 2018, Klaver *et al.*, 2018, Melekhova *et al.*, 2017, Mutch *et al.*, 2019b, Solano *et al.*, 2012, Yanagida *et al.*, 2018).

Studies have suggested that magmas derived from low buoyancy flux plumes such as the Canary Islands (Hoernle & Schmincke, 1993) are dominated by lower crustal storage regions with long repose periods, and residence times of thousands of years at near-solidus conditions (Gleeson *et al.*, 2020, Klügel *et al.*, 2015, Longpré *et al.*, 2014, Longpré *et al.*, 2008, Mutch *et al.*, 2019a). For Tenerife, a reservoir model involving two stages of magmatic fractionation by polybaric differentiation has been suggested by previous researchers (Ablay, 1998, Freundt-Malecha, 2001, Klügel *et al.*, 2015), whereby magmas are extracted sequentially from residual liquids in mushy reservoirs from both a deeper, lower crustal basanitic mush and intermediate-crystallinity (phonotephritic) upper crustal mush, ultimately generating a phonolite liquid (Sliwinski *et al.*, 2015). Las Cañadas phonolites are estimated to have been in the range of 790–850 °C, at ~1 kbar (Andújar *et al.*, 2008, Bryan, 2006, Wolff & Storey, 1983), close to the water-saturated phonolitic minimum (e.g., Hamilton & MacKenzie, 1965). Combined petrological, thermobarometric and geophysical data also indicates that the magmatic system beneath Tenerife is characterised by multi-level magma storage, with melt accumulations inferred at two major crustal discontinuities: a shallow phonolitic body has been recognised at ~5 km (Andújar *et al.*, 2008, Araña *et al.*, 2000, Olin, 2007) extending to oceanic basement at ~8 km b.s.l (Piña-Varas *et al.*, 2018); and a deeper storage region at ~11-14 km, extending across the Moho to ~30 km (Ablay, 1998, Ablay & Kearey, 2000, Borley *et al.*, 1971, Longpré *et al.*, 2008, Martí & Gudmundsson, 2000, Muñoz & Sagredo, 1974, Neumann *et al.*, 1999, Wiesmaier *et al.*, 2013).

Important questions are raised regarding the nature and location of magma bodies at alkalic ocean island volcanoes, and role of crystal-rich (hereafter referred to as ‘mush’) storage systems in the development of major explosive eruptions. Tenerife presents a highly complex and interesting ocean island system, having a heterogeneous mix of volcanic assemblages; encompassing ocean crust, hydrothermal activity and development of evolved felsic rocks in a long-lived volcanic system (Wolff *et al.*, 2000). The 312 ka Fasnia Member (Edgar *et al.* (2017)) provides the opportunity to study a multi-faceted, highly voluminous, well-defined pyroclastic stratigraphy and, in particular the Ravelo ignimbrite, a likely caldera collapse event (Brown *et al.*, 2003, Edgar *et al.*, 2017, Edgar *et al.*, 2007, Stock *et al.*, 2012). The Fasnia Member, of the Diego Hernández Formation, part of the Las Cañadas Upper Group in Tenerife, records the explosive eruption of ~13 km^3 of phonolite magma (Edgar *et al.*, 2007, Olin, 2007). Geochemically the Fasnia Member is highly heterogeneous and contains a large range in trace element compositions; Olin (2007) and Wolff *et al.* (2000) summarised two distinct end member phonolites with a small volume of mafic magma mixing, created a hybrid Fasnia phonolite composition.

Earlier studies have more emphasis on the felsic/phonolitic magma end members which reflect the bulk of the erupting magma. In this paper we focus on the mafic endmember of crystal mush providing insight into the interaction of magmas during the Fasnia Member eruption sequence. Here we present a detailed petrographic and geochemical study of quenched interstitial melts and crystals within juvenile nodules from the Fasnia Member. Unusually, these cumulates contain a high proportion of quenched melt, and all are fresh with no evidence of hydrothermal or post-eruptive alteration. These nodules represent a partially molten crystal mush, quenched on ascent (Stock *et al.*, 2012). Our samples provide a ‘snapshot’ section through the mush system at one well-defined time interval, giving a unique insight into the architecture and dynamics of the magma reservoir. This work provides some of the most detailed empirical constraints on the physicochemical nature of sub-volcanic mush systems to date, thus progressing our understanding of the pre-eruptive assembly of magmatic mush systems. Hence, our findings not only place new chemical and petrological constraints on magma storage conditions beneath Tenerife, but also provide novel information which can help us to understand mush-dominated magmatic systems in other magmatic environments.

GEOLOGICAL BACKGROUND

Magmatism in the Canary volcanic chain in the Eastern Atlantic commenced in the late Cretaceous at ~80 Ma (Balogh *et al.*, 1999, Le Bas *et al.*, 1986b), related to the upwelling of melt 'blobs' in the Canary plume (Hoernle & Schmincke, 1993). Seven volcanic complexes make up the Canary Islands, with Tenerife being the largest with the highest elevation (3718 m.a.s.l; Fig. 1A). As in the other Canary islands, the isotopic and elemental composition of Tenerife is indicative of a young, HIMU (high-μ: $^{238}U/^{204}Pb$) mantle source, suggesting the plume is recycling subducted ocean crust (Hilton *et al.*, 2000, Hoernle & Schmincke, 1993, Hoernle *et al.*, 1991, Simonsen *et al.*, 2000, Thirlwall, 1997). Consistent temporal isotopic variations occurred over the last ~15 Ma of Canary magmatism and are taken to signify chemical variations in the rising plume (Taylor *et al.*, 2020).

Tenerife's earliest phase of activity was dominated by formation of a mafic alkaline basement shield volcano, collectively known as the Old Basaltic Series (subaerially constructed between 12-3.3 Ma; (Ancochea *et al.*, 1990, Fuster, 1968, Martí *et al.*, 1994). This phase was followed by the formation of a central stratovolcano, Las Cañadas, and its volcanic products are split into the Lower and Upper Groups (Araña, 1971). The earliest eruptions were effusive and mafic-intermediate in composition (Lower Group: >3.5 to <2 Ma), but activity became more explosive and felsic in composition from ~2 Ma, involving multiple volcanic cycles and caldera collapse events, as well as flank failures (Ancochea *et al.*, 1999, Araña, 1971, Bryan *et al.*, 1998, Edgar *et al.*, 2002, Martí *et al.*, 1997, Martí *et al.*, 1994). The Upper Group (1.6–0.17 Ma) in order of age, consists of the Ucanca, Guajara and Diego Hernández Formations (Martí *et al.*, 1994). This explosive phase (post 1.84 Ma) includes at least 34 discrete explosive eruptions (Dávila Harris, 2009), which produced widespread phonolitic pyroclastic deposits. These are preserved within the Bandas del Sur pyroclastic apron in the SE of the island, in cliff walls on the SW coast, and within the Las Cañadas caldera wall (Brown *et al.*, 2003, Bryan *et al.*, 2002, Bryan *et al.*, 1998, Dávila Harris, 2009, Edgar *et al.*, 2017, Edgar *et al.*, 2007, Edgar *et al.*, 2002, Martí *et al.*, 1994). Las Cañadas Caldera is defined by a large (16×9 km) summit depression (Fig. 1B), comprised of multiple nested collapse structures, representing a complex evolution involving multiple caldera collapse events (Araña, 1971, Martí, 2019, Martí & Gudmundsson, 2000, Martí *et al.*, 1994). Basaltic volcanism occurred throughout this period with activity focused predominantly along the NE and NW rift systems. The most recent activity on Tenerife developed the post caldera Pico Viejo and Pico Teide (PVPT) basanitic–phonolitic stratovolcanoes, situated within the Las Cañadas caldera (Ablay, 1998, Ancochea *et al.*, 1990, Andújar *et al.*, 2013, Carracedo *et al.*, 2007, Carracedo *et al.*, 2011, Dorado *et al.*, 2021).

One of the largest, most complex and best preserved eruption deposits on Tenerife is the Fasnia Member of the Diego Hernández Formation (Fig.1C), which was emplaced around 312 ka ±6 (Edgar *et al.*, 2017). The Fasnia Member is divided into two distinct eruptive sequences: the Lower and Upper Fasnia (Edgar *et al.*, 2017), containing at least 22 intercalated units, consisting of clast-rich ignimbrites, ash layers and pumice fall deposits (Fig. 1C). The coarse lithic breccia ignimbrite facies (i.e., Ravelo unit) marks a caldera collapse event during the eruption (Edgar *et al.*, 2017, cf. Pittari *et al.*, 2008, Walker, 1981). The approximate total erupted volume of the Fasnia Member is on the order of 62 km^3 of tephra and ~13 km^3 DRE (dense-rock equivalent) magma (Brown *et al.*, 2003, Edgar *et al.*, 2017, Edgar *et al.*, 2007). The deposits are assigned to different schemes (a comparative table of the different stratigraphic schemes is provided in Figure 2 of Edgar *et al.* (2007)), which includes Unit J of Walker (1981), the Lower Grey Member of Bryan *et al.* (1998), the Fasnia

Formation by Brown *et al.* (2003) and the Fasnia Member by Edgar *et al.* (2007). We adopt latter scheme as a continuation of the most recent description of the 20 named members of the Diego Hernández Formation, each representing a major eruption phase (Edgar *et al.*, 2007). A detailed composite stratigraphy and description of the Fasnia Member is given in Edgar *et al.* (2017). Alongside an in-depth geochemical investigation by Olin (2007), these studies describe a complex Plinian sequence which erupted both phonolite and subordinate mafic magmas, preserved by chemically heterogeneous pumice.

Plutonic material is incorporated in many volcanic deposits across the Canary Islands (Barker *et al.*, 2015, Neumann *et al.*, 2000), and a mineralogically diverse suite of plutonic nodules has been identified on Tenerife, including pyroxenitic, gabbroic and syenitic material (Borley *et al.*, 1971, Neumann *et al.*, 2000, Neumann *et al.*, 1999, Pittari *et al.*, 2008, Scott, 1976, Stock *et al.*, 2012, Wolff, 1987). Clinopyroxenes and feldspars within these plutonic lithologies preserve complex major and trace element zoning (both normal and reverse patterns), which have been interpreted as recording periodic magma recharge and mixing events (Bryan *et al.*, 2002, Neumann *et al.*, 1999, Olin, 2007). They commonly preserve thin, highly evolved rim zones, which have been interpreted as recording magma chamber overturn or mixing and amalgamation of two reservoirs in the final stages of crystal growth, shortly before eruption (Neumann *et al.*, 1999, Stock *et al.*, 2012, Triebold *et al.*, 2006). These data have been used as evidence for a compositionally and thermally stratified crustal magma chamber containing low density phonolitic liquids above more dense tephriphonolite, with primitive (i.e., basanitic) melts injecting at the base (Ablay, 1998, Bryan *et al.*, 2002, Martí *et al.*, 2020, Olin, 2007, Stock *et al.*, 2012, Wiesmaier *et al.*, 2013, Wolff, 1985). In this context, the gabbroic nodules have previously been interpreted as disaggregated material from the edges of magma chamber floor and walls (Stock *et al.*, 2012).

ANALYTICAL METHODS

Optical microscopy

Nodule samples were prepared as polished thin sections for petrographic analysis. Whole thin section panoramic photomicrographs were taken in plane (PPL) and cross polarised light (XPL); each photomicrograph comprises between 20 and 200 images taken using a Canon-EOS-60D camera on an Olympus BX-60 polarising microscope. Images were stitched using an individual viewpoint algorithm in the AutoPano Giga (Kolor®) software. The modal mineralogy and vesicle content of 103 juvenile cumulate nodules and eight syenite clasts were determined using the point counting program JMicroVision (Larrea *et al.*, 2014); in each sample, 500 points were counted for coarse grained rocks (average crystal size >2 mm) and 1,000 points counted for finer grained samples. Modal mineral proportions (vol%) for all samples are provided in the Supplementary Data.

Mineral analysis

Backscattered electron images and major element analyses of olivine, clinopyroxene, plagioclase, K-feldspar, feldspathoid, amphibole, biotite, opaques and apatite crystals were collected using a Carl Zeiss Leo 1450VP scanning electron microscope (SEM) in the School of Ocean and Earth Science University of Southampton, equipped with an Oxford Instruments silicon drift energy dispersive spectrometer (EDS). EDS major element data were collected with 20 kV accelerating voltage and the instrument was calibrated using Oxford Instruments factory standards. SEM analyses of all phases are presented in the Supplementary material.

In total, 556 major (>1 wt%) and minor (<1 wt%) element analyses were collected from: 83 clinopyroxene crystals in 17 thin sectioned cumulate samples, using a Cameca SX100 wavelength dispersive electron microprobe (EPMA) in the Department of Earth Sciences, University of Cambridge, and at the School of Earth Sciences, University of Bristol. Mineral analyses were collected using a 15 kV (Cambridge) or 20 kV (Bristol), 20 nA, focussed (~1 μm) beam, with count times 10–30 s for major elements and 30–80 s for minor elements. Analyses with totals outside 98–102 wt% were excluded. Here, we focus on clinopyroxene compositions but other measured mineral compositions are used in bulk nodule composition calculations (data provided in the Supplementary material). To ensure consistency between analytical sessions, analytical uncertainty was monitored through repeat analyses of Smithsonian Microbeam Standards (Jarosewich *et al.*, 1980). In clinopyroxene, relative precision (2σ) is better than ~1–2% for major elements, except Na_2O (± 2.9 %) and FeO (± 4.1 %), and better than ~3–5 % for minor elements, except Cr_2O_3 (± 10.8 %) and MnO (± 34.4 %).

Pyroxene trace element compositions were determined by Laser Ablation Inductively Coupled Plasma-Mass Spectrometry (LA-ICP-MS) using a Thermo Scientific X-Series II coupled to a ESI NWR-193 laser ablation system at the School of Ocean and Earth Science, University of Southampton. Calibration of trace element concentrations was performed using NIST 610, NIST 612, BHVO-2g and BCR-2g, with a secondary correction made using the intensity of ^{43}Ca with known CaO content of the pyroxene determined by electron microprobe. The relative precision of trace element analyses is typically better than 2.5% (2σ), and accuracy is within 5% of recommended values for the reference materials. The relative precision of La/Sm and Dy/Yb ratios is better than 2% and 4%, respectively.

Microcrystalline groundmass analysis

For the groundmass analysis, an aliquot of each nodule was crushed inside a plastic envelope using a non-torque press, before separating 0.5–1.0 mm chips using a Teflon sieve set. This fraction was ultrasonically cleaned in ultra-pure water and dried in a 60 °C oven overnight. Using a binocular microscope, the cleaned rock-chips were visually inspected to remove any fragments with traces of the ignimbrite host, surface staining or cut marks. Quenched melt, i.e., microcrystalline groundmass with no visible phenocrysts, was picked under the microscope and ~0.2–1.0 g of the selected melt chips were ground to a fine powder in an agate pestle and mortar.

Major element analyses were collected on 37 microcrystalline groundmass separates from the Fasnia plutonic nodules by x-ray fluorescence spectroscopy (XRF). For comparison, six bulk-rock samples of pumice and syenite from the Fasnia eruption and an overlying lava flow were also measured. Bulk XRF characterisation of the groundmass was preferred to microanalysis (e.g. EPMA) of the microcrystalline groundmass between acicular quench crystals, primarily to avoid localised fractionation of major elements induced by the rapidly grown quench crystals, but also to reduce the potential for incompatible element-rich minor phases such as apatite, titanite and ilmenite impacting trace element concentrations during growth of microlite phases. Powdered samples were ignited to determine the loss on ignition (LOI) prior to fusion with 0.5 g with dilithium tetraborate flux at 10:1 dilution. Where it was not possible to pick >0.5 g of quenched melt, samples were combined with up to 0.25 g of rock standard JB-3. The melt composition was then deconvoluted from analysis of this gravimetric mixture. Major element analysis was performed using a Philips PW2540 wavelength dispersive XRF in the School of Ocean and Earth Science, University of Southampton. Analytical conditions were similar to those given by Fitton *et al.* (1998); see Table 2. Elements were counted for 20 s (Si, Ti, Fe, Mg), 40 s (Al, Mn, Ca, K, P) or 50 s (Na). Analytical precision was determined from repeat analyses of international secondary standards JB-2, JB-3, BHVO-2, BE-N (Jochum *et al.*, 2005, Kusano *et al.*, 2014) and an in-house reference material (BRR-1). In reference to standard JB-3, 2σ relative standard deviation is <2% for major elements, except P_2O_5 (3.1 %).

Trace element analyses were made on 51 microcrystalline groundmass separates, 16 clinopyroxene separates, nine Fasnia pumices and a basanite lava overlying the Fasnia

Member by ionising coupled plasma-mass spectrometry (ICP-MS). For ICP-MS analyses, 0.1 g of powdered sample was digested using HNO_3-HF, before producing a final 3% HNO_3 solution with dilution factors of 11,700 for the quenched melts and 4,000 for the pumice lava and mafic crystal samples. All measurement solutions were spiked with In and Re as internal standards to monitor drift and bias. Trace element analyses were performed using a Thermo Scientific X-Series II ICP-MS in the School of Ocean and Earth Science, University of Southampton. Data were corrected for interferences and an analytical blank, prior to calibration using a suite of international rock standards (JB-3, JB-1a, JGb-1, BHVO-2, BIR-1, JA-2 (Jochum *et al.*, 2005) and in-house reference material BRR_1. Relative 2σ analytical precision was determined from repeat analyses of international secondary standard JA-2 and is <2.4 % for rare-earth elements (REE), <2% for Zr and 6.5% for Nb (i.e., the elements of interest in this study). Mg and Fe also were measured by ICP-MS, the 2σ relative standard deviation for these elements is <2%.

Complete SEM, EMPA, XRF and ICP-MS datasets along with an assessment of analytical accuracy are provided in Supplementary material. Pyroxene formula recalculations are on a six-oxygen (6O) basis and phase components are defined according to Putirka (2008). Amphibole classification is from Locock (2014). Major and minor elements have been recalculated as atoms per formula unit (a.p.f.u) using the MINERAL software (De Angelis & Neill, 2012). Mg# = [atomic Mg/(Mg + Fe*)], where Fe* = total Fe^{2+} + Fe^{3+}. Forsterite, Fo = [atomic Mg/(Mg + Fe*)] and Anorthite, An = [atomic Na/(Na + Ca + K)].

RESULTS

Occurrence and appearance of the plutonic nodules

We examined 103 melt-bearing plutonic nodules found as pyroclasts in the massive lithic-rich facies of the Ravelo ignimbrite within the Fasnia Member of the Diego Hernández

Formation (Fig. 1). Graphic logs (Fig. 1D-E) and photographs (Fig. 2D) show horizons where the plutonic nodules were sampled in both the caldera wall and distal coastal localities. Equivalent plutonic nodules were also identified as lapilli in the pumice-rich Fasnia fall deposit below the Ravelo lithic breccia. Several horizons of the coarse (blocks and bombs) poorly sorted, lithic breccia facies (Fig. 2B-D) are present in the Ravelo ignimbrite, intercalated with a facies of much finer breccia (lapilli sized clasts; Fig. 2D), interpreted as co-ignimbrite lag breccia deposited in pulses (Edgar *et al.*, 2017). Clast counts from our sampling locations indicate that >70% of Ravelo lithic clasts are angular lapilli and blocks (e.g., Fig. 2A, 2B, 2C) of phonolitic and basaltic lava together with altered sedimentary rocks. Other lithic clasts include variable quantities (8–26%) of syenite, microsyenite and monzodiorite, in which the feldspars are predominately altered to sericite. A full description of clast type, distribution and abundance of these lithic clasts is detailed in (Edgar *et al.*, 2017, Edgar *et al.*, 2007).

As these plutonics are melt-bearing juvenile ejecta, and hence not fully solidified at the time of extraction (Stock *et al.* (2012); Fig. 2E, 2F), the term 'xenolith' is not appropriate; this typically refers to fully solidified or non-erupted plutonic material (Holness *et al.*, 2019). Similarly, the term 'enclave', is used in the literature, but we prefer the term 'nodule' here to describe these plutonic pyroclasts. Plutonic nodules represent 0–4% of the pyroclasts and, alongside the predominantly phonolitic pumice (0–15%), represent the juvenile magmatic clastic material in the ignimbrite. For comparison, samples of the syenite lithic clasts were collected along with unaltered juvenile material.

In hand specimen, the nodules are rounded, dense and characterised by a reflective appearance, generated by fresh crystal facets on their surfaces (Fig. 2F). Nodules range from <1–20 cm in diameter (up to 6 kg) and are generally of similar size to accidental clasts in the same horizon (Fig. 2C, 2D). Nodules can be roughly equigranular but crystal size in individual specimens ranges from ~1–50 mm. Within some nodules, variations in crystal size and modal mineralogy can be seen in hand specimen: some nodules exhibit layering of feldspathic and more mafic components, while others show a visible coarsening of crystals towards domains of microcrystalline groundmass. The microcrystalline groundmass is observed as dull-grey regions within the nodules and occurs within interstitial regions between crystal (areas of 0.1–5 mm) and sub-linear segregations (1–10 cm). Groundmass constitutes 0–60% of the nodules and contains 2–10% vesicles. None of our Fasnia nodules have melt coatings (Fig. 2E, 2F). Instead, a key feature of the more melt-rich nodules is a surface relief generated by upstanding euhedral crystals relative to depressed areas containing melt (Fig. 2F). In some examples, the melt domains show a regmaglyptic development: akin to the dimpled surface of meteorites produced by melt-atmosphere interaction. This is an important feature to consider when interpreting the method of extraction/entrainment of these samples from their plutonic source.

Petrography

The Fasnia juvenile plutonic nodules range from ultramafic to felsic and include wehrlite, clinopyroxenite, pyroxene hornblendite, pyroxene hornblende gabbro, gabbro, and feldspathoid syenite/monzodiorite. Key petrographic features of each lithology are summarised in Table 1 and representative photomicrographs are provided in Supplementary Figure 1. The diversity of Fasnia nodules is depicted in Figure 3, where they are arranged in a stack with downwardly increasing mafic mineral content (i.e., the proportion of olivine, clinopyroxene, amphibole and opaques relative to feldspar, feldspathoid and apatite). Based on changes in modal mineralogy, three broad groups can be distinguished: 1) ultramafic rocks, comprising clinopyroxenites and wehrlites which are plagioclase free; 2) gabbroic rocks, comprising pyroxene hornblende gabbros, hornblende gabbros, and gabbros; and 3) felsic rocks, containing >80% feldspars and feldspathoids, categorised as feldspathoid syenites and monzodiorite. The petrology of these nodule groups and their melt-bearing, microcrystalline groundmass is described below.

Microcrystalline groundmass

The Fasnia plutonic nodules contain 0–60 % microcrystalline groundmass (Table 1) with an average of 26 vol%, weighted by the abundance of each nodule type (Fig. 3). Multiple thin sections from the same specimen show that proportions of microcrystalline groundmass are highly heterogeneous on a decimetre scale, varying by up to ±20 vol%. Approximately 3% of our samples do not contain microcrystalline groundmass, but their phase assemblages, petrography and unaltered mineral preservation, are analogous to other modules and attest to their juvenile origin (we cannot discount that small proportions of groundmass are present in the samples but were missed in our thin sections). Microscopically, the groundmass is observed as microcrystalline, hypocrystalline or hypohyaline material, where the groundmass crystals include acicular amphibole, plagioclase and opaque microlites set in tachylitic glass. Arrays of parallel, needle-like microlites are found propagating from euhedral crystal facets into melt domains (Fig 4A, B). Microcrystalline groundmass is found within the interstitial spaces between crystals (Fig. 4C-D), and as isolated domains or continuous channels bounded by euhedral crystals (Fig. 4F, G). Tracts can cross-cut modal or grain size layering and are sub-perpendicular to any grain alignment, suggesting that they represent sub-vertical pathways through the mush system. These channels are mainly lensoid, but can merge, thin or contain crystal clusters, and vary in width from 0.5–120 mm. Variations in groundmass abundance commonly define layering between crystal-rich and melt-rich domains on a thin-section scale (<5 cm). The groundmass contains spherical vesicles 0.2–6 mm in diameter, but some samples show amorphous vesicle morphology where the gas phase has expanded, displacing melt to occupy the available interstitial space. These textures are characteristic of rapid cooling and decompression, and indicate that microcrystalline groundmass in the nodules was supra-solidus at the time of eruption, and thus can be categorised as 'mush' (Cashman *et al.*, 2017). Microcrystalline groundmass is referred to as interstitial melt, but the term "intercumulus melt" is equally applicable or here is abbreviated to 'melt' when relating to the geochemistry of the plutonic nodules groundmass.

Ultramafic nodules

Wehrlites containing olivine + clinopyroxene + opaques comprise 2% of our nodule samples. Clinopyroxenes (0.3–5.0 mm diameter) exhibit discontinuous concentric zoning, sector zoning (Fig. 5A) or are unzoned. Olivine crystals (0.2–2.0 mm) are dispersed throughout and are euhedral, equant grains, containing <50 μm inclusions of melt and opaques. However, olivine also exists as smaller (0.1–0.4 mm), rounded chadacrysts within clinopyroxene (Fig. 5B). In one sample (L1_89), olivine grains are more abundant adjacent to, or within, the melt pathways and have resorbed rims. Opaques are amorphous and 0.1–0.8 mm in diameter; they occupy intercumulus spaces, together with microcrystalline groundmass.

Clinopyroxenites represent 17% of the nodule suite and contain clinopyroxene and opaques in the proportion ~5:1. One nodule is a biotite clinopyroxenite with ~25% mica (Fig. 5C). Clinopyroxenes (0.5–12.0 mm) are unzoned or occasionally exhibit discrete cores and rims (simple zoning) and/or oscillatory zoning, without evidence of disequilibrium at the crystal rims. Opaques are present as discrete anhedral to subhedral crystals (0.3–5.0 mm; Fig. 5D) and, in some cases, are incorporated in clinopyroxene as parallel, linear opaque inclusion trails (e.g., Fig. 5E). Due to the abundance of opaque minerals, clinopyroxenites are denser than the other nodule samples, with an estimated specific gravity 3.4–3.5 g/cm^3 (from mass balance of the mineral vol%; Table 1). Minor plagioclase (<2%) can be found as microlites in microcrystalline pathways. A common textural feature of the ultramafic nodules is crystals becoming markedly coarser and more euhedral towards melt pathways and segregations (Fig.

5D). This produces hypidiomorphic clinopyroxenes and amphiboles with regular crystal faces formed in contact with melt and irregular faces where in contact with other crystals.

Gabbroic nodules

This group contains plagioclase + clinopyroxene + opaques ± amphibole. Minor apatite, haüyne and K-feldspar are present some samples, with apatite most abundant in amphibole-bearing nodules (<7 vol%; Table 1). Amphibole-bearing lithologies are the most common, comprising 46% and include pyroxene-hornblende gabbros, hornblende pyroxenite, pyroxene hornblendite and hornblende gabbro. Hornblende-free gabbros comprise an estimated 29% of the entire nodule suite.

Plagioclase (0.3–4.5 mm) is tabular and euhedral to subhedral in all gabbroic samples. Smaller plagioclase laths are sometimes present within microcrystalline groundmass regions or filling interstices. Many gabbroic samples contain sieve textured plagioclase, where crystal cores have been invaded and dissolved by melt (Fig. 6A, 6B), occasionally leaving only a skeletal crystal rim. Other plagioclase crystals, including some within the same samples, show no sign of dissolution in the thin section (Fig. 6C). Within this nodule group, clinopyroxene crystals (0.3–6.5 mm) occur as isolated grains or infill dissolved plagioclase cores (Fig. 6D) and can also be sieve textured (Fig. 6E). Many clinopyroxenes have oscillatory and/or sector zonation; in some nodules they contain discrete green cores (in PPL) with abundant small melt and apatite inclusions (Fig. 6F, 6G). In gabbroic nodules with low volumes of microcrystalline groundmass (<5 vol%), crystals are intergrown with irregular grain boundaries (Fig. 6D).

In general, amphibole-bearing nodules are coarsest grained, with crystals up to 50 mm in length. Most amphiboles are euhedral to subhedral and unzoned, but they show evidence of disequilibrium, with sieve-textured cores containing apatite inclusions in a sub-set of nodules.

Gabbroic nodules often exhibit strong shape-preferred orientation of tabular plagioclase and acicular amphibole (Fig. 4C). Combining macro- (hand specimen) and microscopic observations, we find that the shape-preferred orientation defines a strong foliation where elongate crystals are randomly oriented on a single plane in some samples (Fig. 4D, layer 2), whereas others show a lineation with a strong within-plane crystal alignment. Layering is common within individual gabbroic nodules, defined by variations in grain size, grain shape/orientation, groundmass porosity and mineral modal abundance, and multiple layering types can be found in the same sample (Fig. 4D). For example, one feldspathoid-bearing plagioclase-hornblende pyroxenite sample shows distinct modal layering defined by plagioclase-poor, microcrystalline groundmass - and feldspathoid-rich layers with grain alignment, as well as plagioclase-rich, microcrystalline groundmass -poor layers with a weak fabric parallel to the compositional layering (Fig. 4E). In another gabbroic nodule, layering is simultaneously defined by large variations in grain size and groundmass abundance (Fig. 4F).

In both ultramafic and gabbroic nodule groups, melt-rich nodules that lack any fabric or layering typically have coarse, euhedral-subhedral cumulus crystals and often exhibit a large variation of grain-sizes. The largest grains have planar crystallographic growth faces touching microcrystalline groundmass rich-regions (Fig. 5D, 4F-G). Only crystals in contact with the groundmass have a visibly distinct rim colour (e.g., clinopyroxene in Fig. 6E-G). Equally, crystals often form clusters of coalescing grains, with irregular non-planar grain boundaries that form an interlocking 'mosaic' framework, surrounded by microcrystalline groundmass-rich domains containing isolated crystals (Fig. 4G).

Felsic nodules

Felsic feldspathoid syenite/monzodiorite nodules account for ~6% of our sample suite, and contain abundant K-feldspar, with subordinate haüyne + clinopyroxene ± plagioclase (the latter only in monzodiorite). These lithologies contain finer, anhedral crystals (0.2–5.5 mm) compared to the other nodule groups. Groundmass is in low abundance but where present, the microcrystalline groundmass surrounds the crystals (Fig. 4H). K-feldspars (0.2–5.5 mm) often show partial internal dissolution (Fig. 4H) or resorbed rims. Samples contain <12 vol% pale green clinopyroxene crystals (0.3–3.5 mm), which are either unzoned or have simple core–mantle zoning, commonly with opaque inclusions. Haüyne often forms glomeroporphyritic clusters and contains opaque inclusions.

Accidental syenite lithic clasts within the Fasnia pyroclastic deposits are clearly distinct from the felsic juvenile nodules, due to their angularity, nepheline versus haüyne feldspathoids, and the absence of microcrystalline groundmass and extensive hydrothermal alteration of feldspars and feldspathoids to sericite. They are predominantly nepheline syenites and contain K-feldspar, with subordinate nepheline + plagioclase + amphibole + opaques + titanite ± pyroxene (aegirine), with grain sizes ranging 0.2–10 mm. These nepheline syenites are described in detail by Wolff *et al.* (2000) and Edgar *et al.* (2017). The lack of quenched melt or microcrystalline groundmass and hydrothermal alteration below 300°C indicates that these Fasnia syenites rocks were sub-solidus on eruption and hence most likely represent older intrusions (Wolff *et al.*, 2000). Key differences between the juvenile felsic nodules and the accidental syenite lithic blocks are shown in Supplementary Figures 1F-G.

Mineral Chemistry

Chemical analysis of olivine, clinopyroxene, plagioclase, K-feldspar, feldspathoids, amphibole, biotite, opaques and apatite are presented in the Supplementary material. Olivine measured from the wehrlite nodules has forsterite content of Fo_{78-83}. Plagioclase in our nodules varies between An_{44} and An_{88}, in agreement with previous analyses of plagioclase in Tenerife nodules (Stock *et al.*, 2012). K-feldspar measured from sample L1-25 is anorthoclase and we find examples of amphiboles that are classified as kaersutite, measured from sample TR008-20.

Clinopyroxene

Clinopyroxene occurs in (almost) all of our nodules is exclusively titanaugite, as the pyroxenes are Ti-rich (>2.5% TiO_2; Fig. 7A; Table 2). Based on textural and compositional analyses (Fig. 8, Supplementary Figure 3), we identified three distinct clinopyroxene types our juvenile nodules, with varying optical properties in PPL (Fig. 7D-F):

Type-1 clinopyroxenes are Al-rich, generally with a lilac colour in PPL (Fig. 7D). They occur as euhedral-to-subhedral homogenous grains or as mantles around Type-2 green cores (Fig. 7E). These are the most abundant clinopyroxene type in our samples and occur in ~93% of the nodules, including both ultramafic and gabbroic groups. The mean compositions of Type-1 clinopyroxene crystals are similar (including both mantle and rim zones), irrespective of the overall nodule mineralogy (Table 2). However, Type-1 clinopyroxenes span a wider compositional range than types 2 or 3 crystals (although, we acknowledge that this could be due to the higher number of analyses; Fig. 7B). In general, Type-1 crystals are more mafic (higher Mg Number (Mg#) 72-76) than types 2 or 3, with higher TiO_2 and Al_2O_3, and lower Na_2O contents.

Type-2 clinopyroxenes are Fe-rich, which are olive-green colour in PPL (Fig. 7E). They almost exclusively occur as ‘green cores’, encapsulated within Type-1 mantles, but occasionally comprise complete phenocrysts in melt pathways. Type-2 clinopyroxene cores often contain abundant melt and crystal inclusions (e.g., apatite and opaques) giving the dusty appearance. Approximately 12% of the gabbroic and ultramafic nodules contain clinopyroxene crystals Type-2 green cores. They are characterised by low TiO_2 and Al_2O_3 and high Na_2O, MnO and SiO_2 relative to Type-1. Green cores extend to lower Mg# (56-65) and low Al_2O_3 concentrations (1.5-3.0 wt%). Supplementary Figure 3C, D shows transects across crystals containing both Type-1 and Type-2 compositions. Crystals similar to our Type-2 green cores have previously been identified on Tenerife by Scott (1976) and Neumann *et al.* (1999), who classified them as Na-salites and identified two compositional trends and interpreted these as resulting from a fractional crystallisation and mixing.

Type-3 clinopyroxenes are the Al-poor, and are pale green in PPL (Fig. 7F). They occur in ~5% of our nodules and exclusively associated with the felsic group. Type-3 crystals are subhedral–rounded and often contain opaque inclusions. They have an average Mg# of 76 and are distinguished from Type-1 crystals by lower Al_2O_3 and TiO_2 and higher SiO_2, MgO and Na_2O concentrations (Table 2).

An additional clinopyroxene group comprising Na-rich aegirine-augite to aegirine (Fig. 7C) occurs in the Fasnia accidental syenite clasts but is entirely absent from our melt-bearing juvenile nodules (modal mineralogy of syenite clasts are provided in Supplementary material), again attesting to the different origin of these lithics. These are dark green in PPL and occasionally sector zoned (Fig. 7G). They are compositionally distinct from the other clinopyroxene types, with very high Na_2O (up to 10.7 wt%), elevated FeO, SiO_2 and MnO and low CaO and Al_2O_3 concentrations, and Mg# between 6.1–18.6. Aegirine is indicative of late stage- crystallisation from a highly evolved interstitial liquid under high oxygen fugacity and low-pressure conditions (Neumann *et al.*, 1999, Scott, 1976, Yagi, 1966).

Together, the three clinopyroxene types in our juvenile nodules define two peaks in Al KDE (Fig. 8A): a large peak at 0.34 a.p.f.u. and a smaller peak at 0.10 a.p.f.u. The low-Al clinopyroxenes occur in all our nodule lithologies, and include all pyroxene types but are predominantly Type-2 and Type-3 pyroxenes. They have higher Fe*, Na and lower Ca at a given atomic Mg than crystals with high-Al. The high-Al clinopyroxenes occur exclusively in the ultramafic and gabbroic nodule lithologies, which include these Type-1 pyroxenes. A small proportion of crystals from the gabbroic group fall between these two populations but do not define a statistically significant independent KDE peak.

Separating Mg# KDEs by clinopyroxene type (Fig. 8E), the peaks for all Type-1 and Type-3 fall between Mg# 73.6-77.2, with very small differences between Type-1 clinopyroxenes from ultramafic and gabbroic nodules and the Type-3 clinopyroxenes from the felsic lithologies. There are two peaks for Type-2 green cores at Mg# 55.6 and 65.3, which include both ultramafic and gabbroic nodule lithologies. Comparing clinopyroxenes in our nodule samples to crystals from Fasnia pumices, we find that their Mg# coincide. Clinopyroxenes in our nodule samples Mg# is in the range of 53.5–84.2, compares with pyroxenes in Fasnia pumices Mg# 48.2-86.9 (Fig. 8E). Pumice Mg# KDE peaks are at 56.1 and 75.4, with the former aligned with a peak from Type-2 green cores.

Melt and bulk nodule compositions

Interstitial melt chemistry

Microcrystalline interstitial melts in the Fasnia nodules include basanite, trachybasalt, trachy-andesite and trachyte (Fig. 9A; Supplementary material). Unlike the majority of Tenerife volcanics, the interstitial melts follow slightly different alkaline differentiation sequence from basanite towards the phonolite-trachyte boundary. In other words they have a slightly higher silica content at a given alkali content than the majority of Upper Group samples which display a tephrite to phonolite sequence (Ablay, 1998, Ancochea *et al.*, 1990) (grey field in Fig. 9A). The interstitial melts are comparable to the slightly more silica-rich differentiates found in the Old Basaltic Series (Thirlwall *et al.*, 2000). Overall, interstitial melts have an average MgO of 4.4 wt% and a range in MgO 1.1–6 wt% (Fig. 9B-D), average Mg# is ~ 59 (Fig. 3D). A sub-set have higher Al_2O_3 concentrations at a given MgO than is typical for

Tenerife magmas (Fig. 9C); some Fasnia pumices and glasses plus data from other Members of the Diego Hernández Formation (Olin, 2007, Wolff *et al.*, 2000) also have elevated Al_2O_3 concentrations (19.5–23.0 wt%), suggesting the coexistence of a comparable high-Al phonolite.

Interstitial melts from ultramafic nodules have the lowest SiO_2 and total alkalis and highest MgO (mean 5.6 wt% MgO, 43.1 wt% SiO_2, 4.4 wt% $Na_2O + K_2O$, Mg# 61). In contrast, interstitial melts in gabbroic nodules without amphibole (mean 4.5 wt% MgO, 45.1 wt% SiO_2, 5.3 wt% $Na_2O + K_2O$, Mg# 60), hornblende-gabbroic nodules (mean 3.4 wt% MgO, 47.1 wt% SiO_2, 5.9 wt% $Na_2O + K_2O$, Mg# 58) and felsic nodules (mean 2.9 wt% MgO, 52.4 wt% SiO_2, 8.2 wt% $Na_2O + K_2O$, Mg# 53) have successively lower MgO concentrations and in turn, higher concentrations and broader ranges of SiO_2 and total alkalis (Fig. 10A). Where felsic nodules contain quenched interstitial melt, they have the most variable compositions: for example, one sample contains basanitic melt (MgO 4.9 wt%, SiO_2 45.4 wt%, 5.3 wt% $Na_2O + K_2O$) whereas others contain trachytic liquids (1.1–2.5 wt%. MgO, 52.2–59.8 wt%. SiO_2, 8.8-10.7 wt% $Na_2O + K_2O$). Interstitial melts from the ultramafic, gabbroic, hornblende-gabbroic and felsic nodule groups predominantly have Mg# close to the overall average, with 90% having Mg# 54–64 (Fig. 3D). Notably, more melts from hornblende-gabbros and felsic nodules lie below this range, with about a third having Mg# 45–54.

Interstitial melt element variations in different lithological groups are also reflected in their REE ratios. The rare earth element systematics are assessed in Fig. 10B, $[La/Sm]_n$ is used to represent the LREE/MREE (light/middle REE) relationship (c.f. Stock *et al.* (2012)), successively greater $[La/Sm]_n$ ranges are observed in ultramafic, gabbroic, hornblende gabbroic and felsic groups, primarily due to their increasing maximum ratios (Fig. 10B). In contrast, $[Dy/Yb]_n$ (middle/heavy REE; MREE/HREE) ratios have a more limited range in the felsic nodules (1.3–1.6) than mafic and ultramafic groups (1.1–2.2). Overall, interstitial melts from ultramafic and gabbroic nodules have enrichened HREE to LREE patterns typical of Tenerife basaltic magmas ((Wolff *et al.*, 2000); Fig. 11A, B), whereas melts hosted by felsic nodules have slightly more concave REE patterns, with more depletion in elements Pr–Er (Fig. 11C).

Crystal-melt interactions in the different nodule lithologies are explored in Fig. 12A-C, showing the covariations of K_2O, Zr and Eu/Eu* with Al_2O_3. Interstitial melts from all nodules show a general dispersion away from the systematic trend preserved by Tenerife pumice, glasses and whole rocks, towards higher Al_2O_3 at a given K_2O or Zr (Fig. 12B, 12C). Most ultramafic and gabbroic interstitial melts either do not have a negative Eu anomaly or tend towards a slight positive anomaly (Eu/Eu* 0.98–1.06; 12A). Interstitial melt recovered from the felsic nodules have distinctly positive Eu/Eu* (1.06-1.13; Fig. 12A) and is generally the most fractionated with Zr contents 450–590 ppm (Fig. 12B). In comparison, Zr for ultramafic lithologies ranges from 260-450 ppm and gabbroic Zr is in the range of 260-610 ppm. K_2O is particularly high in the interstitial melts of two felsic nodules (Fig. 12C), yet this is not paralleled by a similar increase in Zr (Fig. 12B). Together with their higher Eu/Eu*, this observation suggests that these felsic melts assimilated K-feldspar. A dispersion to high Al_2O_3 and Sr (Fig. 12D, 12E) is particularly noticeable in the gabbroic melts from nodules showing dissolution of plagioclase cores (e.g., L1-69, L1-58, L1-59, L1-3) rather than complete (non-dissolved) plagioclase (e.g., L1-35, L1-37, TEM-05).

Pumice chemistry

Fasnia phonolitic pumices are distinct from any of the Fasnia interstitial melts in being strongly MREE depleted relative to LREE and HREE, (Fig. 11D) with high $[La/Sm]_n$ (8.5–28.5) and low $[Dy/Yb]_n$ (0.4–1.2; Fig. 9E). Pumices have a negative Eu/Eu* (0.46–0.92; Fig 9F). Similar MREE depletion in the Fasnia Member high-Zr phonolites has been attributed to the strong partitioning of MREE into titanite relative to LREE/HREE (Olin & Wolff, 2012).

This MREE depletion could be significantly contributed to by formation of clinopyroxene and amphibole-rich cumulates, as observed in the nodule suite. Fasnia Member phonolites are represented by a low Nb/Zr trend identified by Wolff *et al.* (2000) and Edgar *et al.* (2007). The Fansia pumices form two phonolite groups (high-Zr and low-Zr types, Olin (2007), Wolff *et al.* (2000) and Edgar *et al.* (2007), having a range of Zr contents from 857 – 2110 ppm (Olin, 2007), and correspondingly, values of 1138 – 1669ppm Zr were recorded in this study for Fasnia Member phonolite pumices.

Clinopyroxene equilibrium liquids

Trace elements were measured on representative clinopyroxene bulk separates (via ICP-MS, see methods) from each nodule group and clinopyroxene type. Clinopyroxene REE concentrations were inverted to determine the composition of their equilibrium liquids using distribution coefficients appropriate for alkaline magmas (Fig 11E-H; Supplementary material; (Beard *et al.*, 2019, Wood & Blundy, 1997). This assumes that melt was continuously present during the crystallisation of these clinopyroxenes, and that crystal-liquid partitioning was the dominant concentration-driver, rather than crystal-crystal re-equilibration. Liquids in equilibrium with Type-1 clinopyroxenes in the ultramafic and gabbroic nodules have REE profiles that broadly match the HREE to LREE enrichened REE patterns of interstitial melts (Fig. 11E, 11F). Type-3 clinopyroxenes from felsic nodules (Fig. 11G) are in equilibrium with liquids that have concave REE ($[Dy/Yb]_n$ ~1.2), again broadly matching their interstitial melts, albeit which have slightly lower $[Dy/Yb]_n$. Aegirine clinopyroxene separated from a unaltered nepheline syenite clast are projected to have a strong MREE depletion relative to LREE and HREE (Fig. 11H), comparable to Fasnia phonolitic pumice (Fig. 11D).

Type-2 "green core" clinopyroxenes were not separable from the enveloping Al-rich titanaugite (Type-1), and therefore trace elements were measured by LA-ICP-MS. The centre of the green Type-2 clinopyroxene cores have variable extents of strong MREE depletion ($[Dy/Yb]_n$ 0.3–0.9; Fig. 11H), and HREE enrichment indicating crystallisation from a magma with similar trace element characteristics to the Fasnia pumice and aegirine (Fig. 11H). This produces an array of REE patterns, extending between MREE-depleted, HREE-enriched aegirine crystals and the slightly concave-up Type-3 patterns (Fig. 11G). Similar HREE enrichment and elevated partition coefficients in Fe-rich clinopyroxenes from the Fasnia phonolite are observed by Olin and Wolff (2010).

Calculated bulk nodule compositions

The bulk major element compositions of whole nodule samples can be constrained from their modal proportions and average compositions of mineral and melt phases (Supplementary material). The bulk compositions of >85% of our ultramafic and gabbroic nodules have CaO in the range 13.1–18.4 wt % and elevated MgO at a given TiO_2 or Al_2O_3, which is higher than any previously identified erupted magmas on Tenerife (95% <13 wt% CaO; Fig 9D). These results are comparable to kaersutite-bearing cumulates observed in La Palma lavas (Barker *et al.*, 2015). These compositions can only be developed via the accumulation of clinopyroxene, plagioclase feldspar and amphibole, hence the bulk composition of these mush nodules is unlikely to represent an eruptible composition (Irvine & Yoder, 1979, Jackson, 1967). On this basis, and considering the framework of touching crystals, modal layering, preferred crystal orientation (i.e., a fabric outlined by a shape preferred orientation, c.f. Holness *et al.* (2019)) and disequilibrium textures, the nodules are referred to as cumulates in the sense that they were generated from a differential movement of crystals and liquid, concentrated by crystallisation differentiation (Irvine, 1980).

DISCUSSION

Implications for eruptive processes on Tenerife

Explosive disaggregation and eruption of crystal mush

An important feature of the Fasnia plutonic nodules described above is the lack of any melt coating. If these nodules represent a cumulate mush that had been disaggregated and dislodged by a surge of incoming melt (c.f. Maghdour-Mashhour *et al.*, 2020, Neave *et al.*, 2017, Passmore *et al.*, 2012), which was then carried upwards in this magma, many nodules would then show evidence of this carrier melt on their surfaces or envelopment in a complete carapace. This is likely to be similar in the case of nodules carried into, and mixed with, a felsic reservoir. Carrier melt is present around similar amphibole-bearing cumulate nodules in the 1971 La Palma eruption (Barker *et al.*, 2015) and pyroclastic nodules and xenoliths from Montana Roja on Tenerife (Neumann *et al.*, 2002). Such coatings are partially removed during eruption, but evidence of them should remain in depressions or where the melt infiltrated the crystal mush from the nodule margins. Melt is only present at the surface of the Fasnia nodules where melt domains or channels are truncated. However, the progressive increase in crystal size towards these domains (Fig. 5D) indicates this melt was present during crystal growth and hence is an inherent part of the mush, rather than exogenous infiltration by a carrier. Where this melt is seen at the surface (Fig. 2F) there is evidence that it was preferentially ablated by pneumatic and/or abrasive attrition relative to the coherent crystalline regions. This process would then leave the coarse euhedral crystals on channel margins protruding out of the melt. Hence, we argue that the interstitial melt was most likely to be a liquid during its initial rise in the vent but cooled with the nodule during ballistic ejection and collapse of the eruption column.

Some cumulus crystals preserve a more evolved rim where they are in contact with interstitial melts (e.g., Supplementary Fig. 3; Stock *et al.* (2012)), suggesting late-stage growth from a more intermediate-felsic liquid. However, the lack of a carrier melt of any composition indicates that these rims were not developed following immersion of the nodules in phonolite magma post-fragmentation. This casts doubt on previous explanations for the more evolved rims resulting from the cumulate-rich material being intruded into a felsic reservoir (Triebold *et al.*, 2006), or following overturn of a stratified magma chamber (Stock *et al.*, 2012). Overall, the evidence of rapid cooling, vesiculation and ablation suggests that this inherent melt contained in the nodules was supra-solidus, and that the cumulate mush was 'live' at the time of eruption. The absence of a carrier melt suggests that this mush was in-situ at the time of fragmentation.

The Fasnia eruption is a highly complex Plinian eruption sequence, understood to be partly a consequence of magma-water interactions in the hydrothermal system (Edgar *et al.*, 2017). The Fasnia event comprised of a large volume (>13 km^3 dense magma equivalent) of juvenile erupted material, with an additional >12 km^3 of lithic clasts (Edgar *et al.*, 2017). In addition to juvenile components, the lithic clasts have been interpreted to derive from the roof, walls and conduit, excavated by the explosive eruption (Edgar *et al.*, 2017). Notably, the majority of plutonic lithic clasts are syenitic, with estimates of ~17% syenite clast abundance in the Ravelo ignimbrite (Edgar *et al.*, 2017). This suggests that the plutonic material removed by the eruption from around the phonolitic reservoir was primarily pre-existing syenite, and that altered gabbroic rocks were not a major component in the country rock/wall rock. However, the presence of live mush ejected from a mafic (ultramafic/gabbroic rocks) system implies that explosive fragmentation likely extended below the level of the phonolite reservoir. The observed brittle fracturing of crystals (e.g., Fig. 5B), a texture associated with fragmentation processes (Taddeucci *et al.*, 2022), might also imply that the mafic mush was explosively fragmented. Similarly, deep fragmentation has been proposed for gabbroic and syeno-gabbroid fragments from the 186 ka Abrigo Member (Pittari *et al.*, 2008). Progressive depressurisation during venting of the overlying phonolitic system caused vertical fragmentation (c.f. Brown & Branney, 2004, Edgar *et al.*, 2017, Edgar *et al.*, 2002, Pittari *et al.*, 2008, Smith & Kokelaar, 2013, Vinkler *et al.*, 2012), and we speculate that this mechanism extracted the mafic mush nodules. Because we identified small nodules in the lithic-rich fall deposit (unit F; Fig. 1D) directly below the Ravelo ignimbrite, we infer that the explosive fragmentation of the mush was initiated from the start of the caldera collapse event, as the fall deposit (unit F) interpreted to record the onset of caldera collapse, marking start of the eruption column instability (Edgar *et al.*, 2017).

Structure of the sub-volcanic magma system

Crystal-rich mush stratigraphy

Our petrological analysis indicates that the Fasnia mush system comprised three distinct mineralogical domains: ultramafic, mafic-gabbroic and felsic (Fig. 3). Within the mafic-gabbroic group, some cumulates contain hornblende whilst others do not. This set of 'live' melt-bearing nodules intersects a diverse mineral stratigraphy and gives a detailed insight into the crystal-scale composition of the mush, with the mush containing, on average, 26% melt by volume (Fig. 3). There are no clear correlations between the broad-scale mineralogical divisions in our cumulate suite, the compositions of clinopyroxene crystals or major element chemistry interstitial melt. Additionally, the interstitial melts and clinopyroxene equilibrium liquids have comparable basanitic compositions and Nb/Zr ratios to Las Cañadas mafic lavas and scoria (Wolff *et al.*, 2000) and similar REE patterns through the entire cumulate nodule sequence, with the exception of the evolved pyroxene cores (Fig. 11H). The intercumulus melt REE patterns however, are unlike all Diego Hernández Formation and the majority of Upper Group rocks, showing no evidence of titanite fractionation (Wolff *et al.*, 2000). Nonetheless, there are clear signs of petrological and chemical disequilibrium (discussed below) between phases within each of the mineralogical groupings, indicating periods of magma flux and some degree of overturn in the mush. These broad differences in phase assemblages likely reflect variations in the temperature ±H_2O content of the mush zone (Cooper *et al.*, 2016, Klaver *et al.*, 2017), with ultramafic cumulates stored at higher temperatures than mafic-gabbroic samples, and felsic cumulates stored at low temperatures (i.e., as indicated by the solidus temperatures of their constituent minerals).

Architecture of the Tenerife magma reservoirs

Figure 13 illustrates our representation of the sub-volcanic magmatic system at the time Diego Hernández Formation, alongside geophysical and geobarometic depth estimates derived from previous studies. We will consider the evidence for the vertical extent of the mush and associated magma reservoirs. Alongside the mafic/intermediate melt sampled by our nodule suite, the phonolitic magma end-member reflects the bulk of the erupting magma, existing in a melt-dominated reservoir (Cas *et al.*, 2022, Edgar *et al.*, 2017, Edgar *et al.*, 2007, Edgar *et al.*, 2002, Olin & Wolff, 2012). Phonolites of the Abrigo Member are estimated to be stored at temperatures in the range of 790–850 °C, with pressures corresponding to 4–5 km below surface (Andújar *et al.*, 2008, González-García *et al.*, 2022). Shallow syenitic plutons were emplaced at depths of 4–7 km below the Las Canadas summit, multiple times over the depositional history of the Ucana, Guajara and Diego Hernández Formations (post 1.6 Ma) (Ablay, 1998, Ablay *et al.*, 1995, Bryan *et al.*, 2000, Wolff *et al.*, 2000, Wolff, 1987). Syenite clasts found in the Fasnia and Abrigo ignimbrites are recognised as hydrothermally altered and related to an earlier phase of magmatism (Wolff *et al.*, 2000).

Basanite magma was likely resident in a deeper reservoir (~13–15 km) (Almendros *et al.*, 2007 and references therein), with magmas from Teide and Pico Viejo recording this mantle basanite source (Ablay, 1998). Mafic cumulate body(s) have been identified to exist at depths of 5–14 km below central Tenerife (Ablay & Kearey, 2000, Araña *et al.*, 2000, Neumann *et al.*, 1999). Harzburgite xenoliths coated with basalt carrier melt and found as pyroclasts within the basaltic scoria of Montaña Roja (Neumann *et al.*, 2002), provide physical evidence of this deep mafic reservoir. Interestingly, these mantle assemblages are not observed in the Fasnia nodules. Previous studies have interpreted the mixing of felsic and mafic magma, as evidenced in the Aldea, Fasnia, Poris and Abrigo Members (Bryan *et al.*, 2002, Cas *et al.*, 2022, Edgar *et al.*, 2017, Edgar *et al.*, 2002, González-García *et al.*, 2022, Olin, 2007, Wolff, 1985), an important factor in triggering the phonolitic eruptions in the Diego Hernández Formation. Mafic recharge, melting of felsic cumulates and assimilation of country rock are likely explanations for the creation of highly evolved phonolite and zoned pyroclastic deposits (Wolff *et al.*, 2015, Wolff *et al.*, 2020). Sliwinski *et al.* (2015) hypothesised, that on Tenerife, melts are extracted from residual liquids in mushy reservoirs from both a deeper, basanitic mush and filter into a shallower mush reservoir of intermediate-crystallinity (phonotephritic), ultimately generating a phonolite liquid via a two-step, polybaric differentiation process (Ablay, 1998, Freundt-Malecha, 2001, Klügel *et al.*, 2015).

Pb isotopes of the mafic and felsic volcanics vary in a systematic and coordinated fashion through the last 2 Myr (Taylor *et al.*, 2020). This coordination indicates that primitive magmas fed from the rising Canary plume evolve via crystallisation to generate the bulk of felsic/phonolitic compositions within a timeframe of <50 ka (Taylor *et al.*, 2020), but are likely supplemented by melting and assimilation of syenitic material in the upper crust (Neumann *et al.*, 1999, Sliwinski *et al.*, 2015, Wolff *et al.*, 2000). However, Pb isotopes demonstrate that the Fasnia phonolitic pumice was ultimately derived from a different mantle source (Δ^{208}Pb = 5.9 ± 0.3, n=4; Taylor *et al.* (2020)) to the nodule's interstitial melts (Δ^{208}Pb = 3.8 ± 0.1, n=3; Taylor *et al.* (2020)). This implies that the phonolites were not a *direct* product of crystallisation of the interstitial basanitic melt. It is more probable that the phonolite represents a hybrid magma produced by earlier, higher Δ^{208}Pb mafic/intermediate melts assimilating, or mixing with, older syenitic/phonolitic material (Δ^{208}Pb = 8.0 ± 1.0, n=5; Taylor *et al.* (2020)). However, the isotopic homogeneity of the pumice, irrespective of composition, suggests that rather than assimilation, its isotope composition developed by homogenising magma inputs during its crustal residence time (>20 ka). In this sense, the higher Δ^{208}Pb of the Fasnia phonolite may be weighted towards a slightly older composition of the isotopically dynamic Canary plume (Taylor *et al.*, 2020). Isotopic evidence, coupled with the distinct trace element compositions of the nodule interstitial melts, indicates that the phonolitic magmas were generated in a separate, but coexisting, reservoir to that sampled by the mush nodules.

Our nodule suite provides a detailed (if fragmented) snapshot of the magmatic system immediately prior to a caldera forming eruption. Given our cumulate mush nodules were 'live', in-situ at the time of the eruption and show no indication of hydrothermal alteration and no evidence of felsic melts feeding mafic mush reservoirs, it is logical to place the mafic mush vertically below the phonolite reservoir and syenite plutons (c.f. Pittari *et al.*, 2008). Although our nodule suite includes several felsic cumulates, these typically have low melt fractions which only reach trachyandesitic compositions (Fig. 9A): these liquids are unlikely the parental source of the erupted phonolitic melt. In terms of their major and trace elements, interstitial melts in mafic and felsic nodules are compositionally distinct from the Fasnia pumices and their glasses (Fig. 9), are much more alkali-rich, silica-undersaturated and have bimodal trace element compositions (Zr, Eu/Eu* and REE; Fig. 9E, F, 12B). The trajectory of interstitial melts extends from basanite through to intermediate compositions, lying on a less alkaline trend and are closer to the more silica-rich differentiates found in the Old Basaltic Series (Cas *et al.*, 2022, Thirlwall *et al.*, 2000). The nodules interstitial melts are unrelated to the erupted Fasnia phonolite compositions and do not represent an evolutionary step along the liquid line of descent towards phonolite.

Our data shows that felsic nodules contain basanitic/intermediate melts and have experienced partial dissolution of their crystal framework, which is indicative of an upward migration and reaction of interstitial melt with felsic mush. Similarly, the presence of felsic antecrysts (clinopyroxene cores in equilibrium with a phonolite; Fig. 11H) in gabbroic mush nodules, point to overturn and interaction between the mafic and felsic components during the development of the mush. Such close interaction and exchange between mafic and felsic mush systems suggests that they existed in close proximity, alongside a spatially and isotopically separate, shallow crustal phonolite reservoir (Fig. 13). This configuration would potentially explain the eruption of the mafic and felsic cumulates without a carrier melt, as explosive disaggregation could potentially excavate the heterogeneous mafic-felsic mush resident below the phonolitic reservoir. In many ways, the mafic magmatic system may be similar to other ultramafic-mafic-felsic complexes such as Rum, Scotland. This, relatively shallow complex (3-6 km depth) has a range of cumulate and mineralogical compositions, with some cumulate crystals predicted by barometry to have been transported as a cargo in ascending magmas (Troll *et al.*, 2020). In the case of Tenerife, clinopyroxene barometry suggests their development at 12-25 km (González-García *et al.*, 2022, Neumann *et al.*, 1999), but as observed in the Fasnia nodules they commonly contain cores that are in equilibrium with phonolitic magmas.

Our geochemical data suggests the coexistence of two magma reservoirs, one of phonolite, the other of mafic mush at the time of the Fasnia eruption. However, we have shown that the interstitial melts in the mush were not the primary source of the mafic magma feeding the Fasnia phonolite reservoir. This leaves two possibilities:

(a) The range of nodules was derived from a high-level mushy, differentiated mafic sill complex perched at a high level and incorporated as pyroclasts during fragmentation of the conduit.

(b) two separate crustal reservoirs co-existed but did not significantly mix or cross-feed. The mafic melt responsible for recharge and mixing in the phonolite originated from an isotopically different, earlier phase of magmatism, compared to the melt present in the 'live' mush.

We currently cannot precisely constrain either model within the current uncertainty associated with barometric modelling, thermobarometers are not well experimentally calibrated for alkali systems. The interstitial liquids are not within the calibration ranges for Masotta *et al.* (2013) (suitable for phonolite/trachytic compositions), Neave and Putirka (2017) or Putirka *et al.* (1996). As with the Rum intrusion, pyroxene barometry is likely to put crystallisation depths significantly below the emplacement depth (Troll *et al.*, 2020). Overall, depth estimates for the nodule formation are difficult given the limitations and degree of uncertainty associated with barometric modelling in alkaline magmas, their interaction with felsic material, chemical distinction from the erupting phonolite magma and an origin from explosive fragmentation. Without any well constrained depth estimates, the vertical extent and architecture of this system that the nodules represent cannot be perfectly constrained. It is feasible that mush compositions grade stratigraphically through the crust and the nodules represent samples from the mid- to upper-crust, or alternatively the nodules are derived from a differentiated, dominantly mafic sill mush complex/complexes. We favour the first hypothesis, that is, that these nodules represent a mid-crustal mush, being fed by magmas ascending from the deep basanite reservoir. A further avenue of work would be to investigate the Pb isotope systematics of the systems components, i.e. the mush melts and crystals together with the phonolitic liquids. This would provide information on the diversity, origin, interaction and relative age of magmas present in Fasnia times.

Crystallisation and development of the mush

Crystallisation environments

The range of cumulate textures and mineral zonation observed in the nodules described in the results above record different crystallisation environments that existed at the time of the Fasnia eruption. Although disaggregated nodules lack the spatial context available in layered intrusions (e.g., Holness *et al.*, 2019), two distinct modes of crystallisation are recognised from our mafic nodule suite: 1) *in situ* growth of a static crystal meshwork; 2) crystal deposition in a liquid-rich magma body. These are outlined below:

In situ growth – Some pyroxenitic, wehrlitic and gabbroic nodules have partially to fully interlocking grains with mosaic textures, representing a progression from mesocumulate towards adcumulate with diminishing interstitial melt. These textures, where grains have grown to impingement (i.e., they have non-planar and interlocking boundaries), are thought to have crystallised within a static crystal zone (Holness *et al.*, 2019). Clinopyroxenes are typically un-zoned but can show simple zoning where crystal faces were in contact with melt (e.g., narrow rim zones; Supplementary Fig. 2C-D), sector zoning and/or oscillatory zoning (Fig. 5A, 6E). A small number of the cumulates contain only minor melt-filled interstices and are dominated by interpenetrating crystals with highly irregular boundaries. These often preserve evidence of resorption at, or close to their rims, suggesting reaction with late-stage melts. In these nodules, there is no evidence of sub-solidus deformation, grain alignment or crystal reorganisation within a magmatic flow, and they are therefore consistent with *in situ* meshwork crystallisation (Holness *et al.*, 2019, Sparks *et al.*, 1985). However, these cumulates typically exhibit wide-ranging grain sizes, with progressively larger and more euhedral crystals (5–20 mm) adjacent to melt-rich domains (Fig. 4F, 5D), possibly indicating progressive channelized melt flow through during crystallisation.

Crystal deposition in a liquid-rich magma body – Gabbroic nodules, particularly those with high abundances of amphibole and plagioclase, often preserve a strong mineral alignment (Fig. 4C, D). This fabric is indicative of crystals developing specific coordinated orientations by fluid dynamical processes within a liquid-rich magma body (Holness *et al.*, 2019). Euhedral crystals and crystal clusters surrounded by melt also provide evidence for a liquid-rich environment (Fig. 4F, G). Some samples show foliation (Fig. 4C), where crystals settled out from a liquid onto an accumulation surface with random alignment in this plane, indicative of a static melt domain. In other nodules, crystals are co-aligned on accumulation surfaces, which is indicative of crystal settling within a magma current or mass movement of a crystal mush layer (Holness *et al.*, 2019, Hunter, 1996, Irvine, 1980, Wager *et al.*, 1960). These samples typically preserve phase/modal/grain size layering, with relatively uniform grain-size distributions within individual layer(s) (Fig. 4D). This layering could result from a range of dynamic or non-dynamic processes, including crystal re-arrangement from a flow, crystal segregation from convective liquid movement, magma injection causing stratification and/or mixing and crystallisation conditions changing rapidly (Namur *et al.*, 2015).

Felsic nodules exhibit a narrower range in grain sizes than our more mafic nodules and, where present, melt surrounds the cumulus crystals (Fig. 4H, Supplementary Fig. 1F). Here, the form of the grain boundaries and crystal faces is obscured by rim dissolution and overgrowth, making the crystallisation environment challenging to interpret.

Melt movement and reaction in the mush

Gabbroic nodules (including amphibole-bearing cumulates) typically exhibit complex and variable petrographic textures (Fig. 6A-D), including disequilibrium crystal textures (e.g., resorbed or skeletal plagioclase, relic cores, irregular grain boundaries; Fig 6A, 6B) and disaggregated cumulus grains, where crystals derived from the mush are surrounded by melt (e.g., within channels or melt pockets; Fig. 4G). Here, the zoned crystals and diverse crystal populations provide evidence for open-system mixing (Schleicher & Bergantz, 2017). Dissolved plagioclase cores will contain remnant fragments of the original plagioclase, resulting in skeletal, sieve or pixelated textures (Fig. 6A, samples L1-69, L1-58). Overall, these observations point to melt moving through the mafic mush instigating reactive dissolution of plagioclase cores. This process resulted in modified melt compositions that evolved to be in equilibrium with the crystals before full dissolution (Geist *et al.*, 2014, Geist *et al.*, 2005). A consequence of this mineral-specific reactive flow was the generation of melts with increased Al_2O_3 and Sr contents (Fig. 12E) and positive Eu anomalies (Fig. 12A). Furthermore, the high-Al_2O_3 melts require our picked (and XRF analysed) groundmass glasses to locally contain 10–20% more plagioclase than a typical Tenerife liquid, which is not supported by SEM photomicrographs of our nodule samples (Fig. 4A, B). While the felsic interstitial melt compositions extend to high K_2O and may have accumulated K-feldspar, the gabbroic nodule interstitial melt trend towards high Al_2O_3, indicating assimilation of plagioclase. Gabbroic interstitial melts show weakly positive correlations between Al_2O_3–Zr and Al_2O_3–K_2O, which alongside their differing REE abundances, suggests that the interstitial melts are variably fractionated. Positive Eu anomalies in both lithologies is viewed as a signal of cumulate melting in felsic systems (Wolff *et al.*, 2020).

We interpret these resorption features as recording an open magmatic system, characterised by periods of mature, orthocumulate crystallisation where interstitial melts are isolated by an impermeable crystal network and infill pore space within the mush, punctuated by periods of reactive melt infiltration and circulation (Gleeson *et al.*, 2020, Sparks *et al.*, 1985). Our cumulates can show evidence for multi-stage formation, where new melts that infiltrate the mush — either along grain boundaries or channels — are in disequilibrium with pre-existing cumulates, dissolving crystal phases and recrystallizing new equilibrium phases (Fig. 6D). We observe evidence for chemical and textural zonation in the mafic mush with elevated Al_2O_3 and Sr in the intermediate melts residing in the interstitial regions, supporting the process of cognate cumulate melting or 'feldspar cannibalization' suggested by Wolff *et al.* (2015) and Sliwinski *et al.* (2015). The structure of melt domains within the cumulates suggests melt infiltration was highly localised, within mm-scale channels, and that the impact of reactive melts would, therefore, be spatially variable on short length scales (c.f. Spiegelman & Kelemen, 2003), affecting different parts of the mush at different points in time. This helps explain the lack of a correlation between the broad-scale lithological divisions in our nodule suite, the compositions of clinopyroxene crystals and the major element chemical characteristics of the interstitial melt.

Our Type-2 crystals are characterised by Mg# <60 and strong MREE depletion, which testify to their equilibrium liquids having already experienced a high degree of pyroxene, amphibole, and apatite and potentially titanite removal (Ablay, 1998, Olin & Wolff, 2012). Negative Eu anomalies also indicate that their equilibrium melts had previously crystallised, or were co-precipitating, feldspar (Ablay, 1998, Sliwinski *et al.*, 2015). These features implicate crystallisation from an evolved liquid, in agreement with previous interpretations of analogous green clinopyroxene in other Tenerife eruptions, which are thought to be antecrystic, having formed from low temperature phonolitic melts prior to incorporation into more basanitic magmas (Duda & Schmincke, 1985, Neumann *et al.*, 1999). Type-2 clinopyroxenes are not in equilibrium with the interstitial melts in their ultramafic and gabbroic host cumulates, and are typically encapsulated in the more primitive Type-1 clinopyroxenes, which could have developed during a period of destabilisation following an influx of mafic magma into their growth environment e.g. (Cashman *et al.*, 2017, Christopher *et al.*, 2015). Gabbroic nodules containing green core clinopyroxene also commonly contain abundant skeletal plagioclase, where crystal cores have been resorbed by interstitial melts (Fig. 6A; exemplified in samples L1-59, L1-58, L1-69, L1-78, TEM-01, TEM-05-02). These plagioclase phenocrysts have low anorthite contents ($<60_{An}$; Stock *et al.* (2012)) and we suggest that they co-precipitated in an evolved magma body alongside the Type-2 clinopyroxenes. However, in contrast with the plagioclase, the Type-2 clinopyroxenes do not show evidence of resorption. Felsic-mush derived Type-2 green cores could originate from: 1) disaggregation and incorporation of a pre-existing felsic mush body during the development of a new mafic magma reservoir; 2) a pocket/roof-zone of evolved melt within a larger mafic reservoir which was recycled during an overturn event; 3) a deeper felsic magma reservoir (Stock *et al.*, 2020) or 4) xenocrysts transported from phonolitic melts produced by a carbonatite-lherzolite reaction in the mantle (Loges *et al.*, 2019). The latter origin is difficult to reconcile with the feldspar + pyroxene crystallisation history (MREE depletion), evident from the green core trace element equilibrium liquid compositions (Fig. 11H). We find it more plausible that the antecrystic Type-2 clinopyroxene cores grew in a zone of felsic mush prior to mobilisation and incorporation into an expanding gabbroic mush, based on: (i) the continuum of cumulate lithologies we observe in our nodule samples; (ii) the abundance of low Mg# evolved clinopyroxenes and low An# plagioclase cores; (iii) the cores in equilibrium with a phonolite; (Fig. 11H), and (iv) the presence of both mafic and felsic cumulate mush nodules in the products of same eruption. It is possible that the evolved crystal growth environment was only ephemeral and formed through structural reorganisation of the mush zone (e.g., Druitt *et al*. 2012, Christopher *et al*. 2015).

We suggest that, while the mush system is petrographically zoned it is heterogeneous in its lithologies and crystal chemistries, containing liquid-rich and crystal-rich regions and is periodically flushed by ascending, reactive melts. These observations are consistent with recent models of transcrustal, interconnected magma storage regions (Bachmann & Bergantz, 2004, Cashman *et al.*, 2017, Christopher *et al.*, 2015, Marsh, 2004) and provide empirical evidence for this type of magma mush system architecture at a major ocean island volcano.

CONCLUSIONS

Petrographic and geochemical analysis of melt-bearing cumulate mush nodules provides an insight into the architecture and dynamics of the sub-volcanic system at the time of the 312 ka Fasnia eruption. The nodules provide a detailed insight into the crystal-scale makeup of the mush, covering a broad lithological range including ultramafic, mafic-gabbroic and felsic cumulates which, as a whole, contain an average of 26% melt. They represent petrographic zoning through the entire mush column, with ubiquitous evidence of melt mobility though channels and segregations. Interstitial movement of reactive melts is apparent from crystal disequilibria in feldspars through mafic and felsic cumulates. Preferential dissolution of plagioclase and anorthoclase feldspars by reactive interstitial melts may be responsible for the high-Al characteristics of magmas in the mush system, observed in the interstitial melts. Critically, interstitial melts and clinopyroxene compositions in different nodules from the mush do not show any correlation with their host cumulate mineralogy, suggesting that the system was in a broad state of disequilibrium. Interstitial melt compositions are broadly similar through the mafic/felsic nodule lithologies, indicating they are relatively well-mixed and connected. However, these melts have a clearly distinct composition compared to the phonolitic magmas driving the Fasnia eruption, suggesting the coexistence of two discrete magma reservoirs. Given the melt-rich supra-solidus nature of the cumulates, combined with the lack of a carrier melt around the nodules, the active mafic mush reservoir is likely to have been explosively fragmented from its crustal position beneath the coexisting evolved phonolite magma body. More work is needed to quantitatively assess the stratigraphic depth of origin for these mush nodules, a thermobarometric approach, suitable for alkaline systems with a high degree of accuracy is required in separate the geometry of the multiple reservoirs present in this complex magmatic system.

ACKNOWLEDGEMENTS

This work was supported by the Natural Environmental Research Council [grant number NE/L002531/1] and access to sites within the National Park granted by the Administration of the Teide National Park. MJS acknowledges additional support from a Frontiers for the Future grant [20/FFP-P/8895], co-funded by Science Foundation Ireland and Geological Survey Ireland. Andy Milton, Agnes Michalik, Matt Cooper, Iris Buisman, Ellie Hayward and Katie Schofield are thanked for laboratory assistance. Thanks to Otto Karhunen and Tim Wollen for contributing to trace element analysis, many thanks to Emma Watts for fieldwork assistance and support. John Wolff, Joan Martí, Ben Ellis and an anonymous reviewer are thanked for their time and valuable input in improving the manuscript during the review process.

DATA AVAILABILITY

The original data generated in this study and underlying this article is available in its online supplementary material. Third party datasets included in the article were derived from sources in the public domain (GEOROC, http://georoc.mpch-mainz.gwdg.de/georoc/).

REFERENCES

Ablay, G. J., Carroll, M.R., Palmer, M.R., Martí, J. and Sparks, R.S.J., . (1998). Basanite–phonolite lineages of the Teide–Pico Viejo volcanic complex, Tenerife, Canary Islands. *Journal of petrology* **39(5)**, 905-936.

Ablay, G. J., Ernst, G. G. J., Marti, J. & Sparks, R. S. J. (1995). The ~2 ka subplinian eruption of Montaña Blanca, Tenerife. *Bulletin of Volcanology* **57**, 337-355.

Ablay, G. J. & Kearey, P. (2000). Gravity constraints on the structure and volcanic evolution of Tenerife, Canary Islands. *Journal of Geophysical Research: Solid Earth* **105**, 5783-5796.

Almendros, J., Ibáñez, J. M., Carmona, E. & Zandomeneghi, D. (2007). Array analyses of volcanic earthquakes and tremor recorded at Las Cañadas caldera (Tenerife Island, Spain) during the 2004 seismic activation of Teide volcano. *Journal of Volcanology and Geothermal Research* **160**, 285-299.

Ancochea, E., Fuster, J., Ibarrola, E., Cendrero, A., Coello, J., Hernan, F., Cantagrel, J. M. & Jamond, C. (1990). Volcanic evolution of the island of Tenerife (Canary Islands) in the light of new K-Ar data. *Journal of Volcanology and Geothermal Research* **44**, 231-249.

Ancochea, E., Huertas, M., Cantagrel, J. M., Coello, J., Fúster, J., Arnaud, N. & Ibarrola, E. (1999). Evolution of the Cañadas edifice and its implications for the origin of the Cañadas Caldera (Tenerife, Canary Islands). *Journal of Volcanology and Geothermal Research* **88**, 177-199.

Andújar, J., Costa, F., Martí, J., Wolff, J. & Carroll, M. (2008). Experimental constraints on pre-eruptive conditions of phonolitic magma from the caldera-forming El Abrigo eruption, Tenerife (Canary Islands). *Chemical Geology* **257**, 173-191.

Andújar, J., Costa, F. & Scaillet, B. (2013). Storage conditions and eruptive dynamics of central versus flank eruptions in volcanic islands: the case of Tenerife (Canary Islands, Spain). *Journal of Volcanology and Geothermal Research* **260**, 62-79.

Araña, V. (1971). Litología y estructura del Edificio Cañadas, Tenerife (Islas Canarias). *Estudios geológicos* **27**, 95-135.

Araña, V., Camacho, A., Garcia, A., Montesinos, F., Blanco, I., Vieira, R. & Felpeto, A. (2000). Internal structure of Tenerife (Canary Islands) based on gravity, aeromagnetic and volcanological data. *Journal of Volcanology and Geothermal Research* **103**, 43-64.

Bachmann, O. & Bergantz, G. W. (2004). On the origin of crystal-poor rhyolites: extracted from batholithic crystal mushes. *Journal of petrology* **45**, 1565-1582.

Bachmann, O. & Bergantz, G. W. (2008). Rhyolites and their source mushes across tectonic settings. *Journal of petrology* **49**, 2277-2285.

Balogh, K., Ahijado, A., Casillas, R. & Fernandez, C. (1999). Contributions to the chronology of the Basal Complex of Fuerteventura, Canary Islands. *Journal of Volcanology and Geothermal Research* **90**, 81-101.

Barker, A. K., Troll, V. R., Carracedo, J. C. & Nicholls, P. A. (2015). The magma plumbing system for the 1971 Teneguía eruption on La Palma, Canary Islands. *Contributions to Mineralogy and Petrology* **170**, 1-21.

Beard, C. D., van Hinsberg, V. J., Stix, J. & Wilke, M. (2019). Clinopyroxene/melt trace element partitioning in sodic alkaline magmas. *Journal of petrology* **60**, 1797-1823.

Borley, G., Suddaby, P. & Scott, P. (1971). Some xenoliths from the alkalic rocks of Teneriffe, Canary Islands. *Contributions to Mineralogy and Petrology* **31**, 102-114.

Brown, R., Barry, T., Branney, M., Pringle, M. & Bryan, S. (2003). The Quaternary pyroclastic succession of southeast Tenerife, Canary Islands: explosive eruptions, related caldera subsidence, and sector collapse. *Geological Magazine* **140**, 265-288.

Brown, R. J. & Branney, M. J. (2004). Event-stratigraphy of a caldera-forming ignimbrite eruption on Tenerife: the 273 ka Poris Formation. *Bulletin of Volcanology* **66**, 392-416.

Bryan, S., Cas, R. & Martı, J. (2000). The 0.57 Ma plinian eruption of the Granadilla Member, Tenerife (Canary Islands): an example of complexity in eruption dynamics and evolution. *Journal of Volcanology and Geothermal Research* **103**, 209-238.

Bryan, S., Marti, J. & Leosson, M. (2002). Petrology and geochemistry of the bandas del Sur formation, Las Cañadas edifice, Tenerife (Canary Islands). *Journal of petrology* **43**, 1815-1856.

Bryan, S. E. (2006). Petrology and geochemistry of the Quaternary caldera-forming, phonolitic Granadilla eruption, Tenerife (Canary Islands). *Journal of petrology* **47**, 1557-1589.

Bryan, S. E., Martí, J. & Cas, R. A. (1998). Stratigraphy of the Bandas del Sur Formation: an extracaldera record of Quaternary phonolitic explosive eruptions from the Las Cañadas edifice, Tenerife (Canary Islands). *Geological Magazine* **135**, 605-636.

Carracedo, J. C., Badiola, E. R., Guillou, H., Paterne, M., Scaillet, S., Torrado, F. P., Paris, R., Fra-Paleo, U. & Hansen, A. (2007). Eruptive and structural history of Teide Volcano and rift zones of Tenerife, Canary Islands. *Geological Society of America Bulletin* **119**, 1027-1051.

Carracedo, J. C., Guillou, H., Nomade, S., Rodríguez-Badiola, E., Pérez-Torrado, F. J., Rodríguez-González, A., Paris, R., Troll, V. R., Wiesmaier, S. & Delcamp, A. (2011). Evolution of ocean-island rifts: The northeast rift zone of Tenerife, Canary Islands. *Bulletin* **123**, 562-584.

Cas, R. A., Wolff, J. A., Marti, J., Olin, P. H., Edgar, C. J., Pittari, A. & Simmons, J. M. (2022). Tenerife, a complex end member of basaltic oceanic island volcanoes, with explosive polygenetic phonolitic calderas, and phonolitic-basaltic stratovolcanoes. *Earth-Science Reviews*, 103990.

Cashman, K. V., Sparks, R. S. J. & Blundy, J. D. (2017). Vertically extensive and unstable magmatic systems: a unified view of igneous processes. *Science* **355**, eaag3055.

Christopher, T., Blundy, J., Cashman, K., Cole, P., Edmonds, M., Smith, P., Sparks, R. & Stinton, A. (2015). Crustal-scale degassing due to magma system destabilization and magma-gas decoupling at Soufrière Hills Volcano, Montserrat. *Geochemistry, Geophysics, Geosystems* **16**, 2797-2811.

Cooper, G. F., Davidson, J. P. & Blundy, J. D. (2016). Plutonic xenoliths from Martinique, Lesser Antilles: evidence for open system processes and reactive melt flow in island arc crust. *Contributions to Mineralogy and Petrology* **171**, 1-21.

Dávila Harris, P. (2009). Explosive ocean-island volcanism: the 1.8–0.7 Ma explosive eruption history of Cañadas volcano recorded by the pyroclastic successions around Adeje and Abona, southern Tenerife, Canary Islands. University of Leicester.

Dorado, O., Andújar, J., Martí, J. & Geyer, A. (2021). Pre-eruptive conditions at satellite vent eruptions at Teide-Pico Viejo complex (Tenerife, Canary Islands). *Lithos* **396**, 106193.

Duda, A. & Schmincke, H.-U. (1985). Polybaric differentiation of alkali basaltic magmas: evidence from green-core clinopyroxenes (Eifel, FRG). *Contributions to Mineralogy and Petrology* **91**, 340-353.

Edgar, C., Cas, R. A., Olin, P., Wolff, J., Martí, J. & Simmons, J. (2017). Causes of complexity in a fallout dominated plinian eruption sequence: 312 ka Fasnia Member, Diego Hernández Formation, Tenerife, Spain. *Journal of Volcanology and Geothermal Research* **345**, 21-45.

Edgar, C., Wolff, J., Olin, P., Nichols, H., Pittari, A., Cas, R., Reiners, P. W., Spell, T. & Martí, J. (2007). The late Quaternary Diego Hernandez Formation, Tenerife: Volcanology of a complex cycle of voluminous explosive phonolitic eruptions. *Journal of Volcanology and Geothermal Research* **160**, 59-85.

Edgar, C., Wolff, J. A., Nichols, H. J., Cas, R. A. & Martı, J. (2002). A complex Quaternary ignimbrite-forming phonolitic eruption: the Poris member of the Diego Hernández Formation (Tenerife, Canary Islands). *Journal of Volcanology and Geothermal Research* **118**, 99-130.

Edmonds, M., Cashman, K. V., Holness, M. & Jackson, M. (2019). Architecture and dynamics of magma reservoirs. The Royal Society Publishing.

Evensen, N., Hamilton, P. & O'nions, R. (1978). Rare-earth abundances in chondritic meteorites. *Geochimica et Cosmochimica Acta* **42**, 1199-1212.

Fitton, J., Saunders, A., Larsen, L., Hardarson, B. & Norry, M. (1998). Volcanic Rocks from the South East Greenland Margin at 63 N: Composition, petrogenesis and mantle sources. *Proceedings of the Ocean Drilling Program: Scientific Results*: Ocean Drilling Program, 331.

Freundt-Malecha, B. (2001). Plutonic rocks of intermediate composition on Gran Canaria: the missing link of the bimodal volcanic rock suite. *Contributions to Mineralogy and Petrology* **141**, 430-445.

Fuster, J. M. (1968). *Geología y volcanología de las Islas Canarias: Tenerife*: CSIC, Instituto Lucas Mallada.

Geist, D. J., Bergantz, G. & Chadwick, W. W. (2014). Galápagos magma chambers. *The Galapagos: A natural laboratory for the Earth sciences* **204**, 55-70.

Geist, D. J., Naumann, T. R., Standish, J. J., Kurz, M. D., Harpp, K. S., White, W. M. & Fornari, D. J. (2005). Wolf Volcano, Galápagos Archipelago: Melting and magmatic evolution at the margins of a mantle plume. *Journal of petrology* **46**, 2197-2224.

Gleeson, M. L., Gibson, S. A. & Stock, M. J. (2020). Upper mantle mush zones beneath low melt flux ocean island volcanoes: insights from Isla Floreana, Galápagos. *Journal of petrology* **61**.

González-García, D., Petrelli, M., Perugini, D., Giordano, D., Vasseur, J., Paredes-Mariño, J., Marti, J. & Dingwell, D. B. (2022). Pre-eruptive conditions and dynamics recorded in banded pumices from the El Abrigo caldera-forming eruption (Tenerife, Canary Islands). *Journal of petrology* **63**, egac009.

Hamilton, D. & MacKenzie, W. (1965). Phase-equilibrium studies in the system NaAlSiO4 (nepheline)–KAlSiO4 (kalsilite)–SiO2-H2O. *Mineralogical magazine and journal of the Mineralogical Society* **34**, 214-231.

Hilton, D., Macphersona, C. & Elliottb, T. (2000). Helium isotope ratios in mafic phenocrysts and geothermal fluids from La Palma, the Canary Islands (Spain): implications for HIMU mantle sources. *Geochimica et Cosmochimica Acta* **64**, 2119-2132.

Hoernle, K. & Schmincke, H.-U. (1993). The role of partial melting in the 15-Ma geochemical evolution of Gran Canaria: a blob model for the Canary hotspot. *Journal of petrology* **34**, 599-626.

Hoernle, K., Tilton, G. & Schmincke, H.-U. (1991). SrNdPb isotopic evolution of Gran Canaria: Evidence for shallow enriched mantle beneath the Canary Islands. *Earth and Planetary Science Letters* **106**, 44-63.

Holness, M. B., Stock, M. J. & Geist, D. (2019). Magma chambers versus mush zones: constraining the architecture of sub-volcanic plumbing systems from microstructural analysis of crystalline enclaves. *Philosophical Transactions of the Royal Society A* **377**, 20180006.

Hunter, R. (1996). Texture development in cumulate rocks. *Developments in Petrology*: Elsevier, 77-101.

Irvine, T. (1980). Magmatic density currents and cumulus processes. *American Journal of Science* **280**, 1-58.

Irvine, T. & Yoder, H. (1979). Rocks whose composition is determined by crystal accumulation and sorting. *The evolution of the igneous rocks: fiftieth anniversary perspectives*, 245-306.

Jackson, E. (1967). Ultramafic cumulates in the Stillwater, Great Dyke, and Bushveld intrusions. *Ultramafic and related rocks*, 20-38.

Jackson, M., Blundy, J. & Sparks, R. (2018). Chemical differentiation, cold storage and remobilization of magma in the Earth's crust. *Nature*, 1.

Jarosewich, E., Nelen, J. & Norberg, J. A. (1980). Reference samples for electron microprobe analysis. *Geostandards Newsletter* **4**, 43-47.

Jeffery, A. J. & Gertisser, R. (2018). Peralkaline Felsic Magmatism of the Atlantic Islands. *Frontiers in Earth Science* **6**.

Jochum, K. P., Nohl, U., Herwig, K., Lammel, E., Stoll, B. & Hofmann, A. W. (2005). GeoReM: a new geochemical database for reference materials and isotopic standards. *Geostandards and Geoanalytical Research* **29**, 333-338.

Klaver, M., Blundy, J. D. & Vroon, P. Z. (2018). Generation of arc rhyodacites through cumulate-melt reactions in a deep crustal hot zone: Evidence from Nisyros volcano. *Earth and Planetary Science Letters* **497**, 169-180.

Klaver, M., Matveev, S., Berndt, J., Lissenberg, C. J. & Vroon, P. Z. (2017). A mineral and cumulate perspective to magma differentiation at Nisyros volcano, Aegean arc. *Contributions to Mineralogy and Petrology* **172**, 95.

Klügel, A., Longpré, M.-A., García-Cañada, L. & Stix, J. (2015). Deep intrusions, lateral magma transport and related uplift at ocean island volcanoes. *Earth and Planetary Science Letters* **431**, 140-149.

Kusano, Y., Umino, S., Kobayashi, J., Mizukami, T., Okuno, M. & Arai, S. (2014). Quantitative analysis of major elements in igneous rocks with X-ray fluorescence spectrometer "ZSX primus II" using a 1: 10 dilution glass bead. *Sci. Rep. Kanazawa Univ* **58**, 31-44.

Larrea, M. L., Castro, S. M. & Bjerg, E. A. (2014). A software solution for point counting. Petrographic thin section analysis as a case study. *Arabian Journal of Geosciences* **7**, 2981-2989.

Le Bas, M., Le Maitre, R., Streckeisen, A., Zanettin, B. & Rocks, I. S. o. t. S. o. I. (1986a). A chemical classification of volcanic rocks based on the total alkali-silica diagram. *Journal of petrology* **27**, 745-750.

Le Bas, M., Rex, D. & Stillman, C. (1986b). The early magmatic chronology of Fuerteventura, Canary Islands. *Geological Magazine* **123**, 287-298.

Locock, A. J. (2014). An Excel spreadsheet to classify chemical analyses of amphiboles following the IMA 2012 recommendations. *Computers & Geosciences* **62**, 1-11.

Loges, A., Schultze, D., Klügel, A. & Lucassen, F. (2019). Phonolitic melt production by carbonatite Mantle metasomatism: evidence from Eger Graben xenoliths. *Contributions to Mineralogy and Petrology* **174**, 1-24.

Longpré, M.-A., Klügel, A., Diehl, A. & Stix, J. (2014). Mixing in mantle magma reservoirs prior to and during the 2011–2012 eruption at El Hierro, Canary Islands. *Geology* **42**, 315-318.

Longpré, M. A., Troll, V. R. & Hansteen, T. H. (2008). Upper mantle magma storage and transport under a Canarian shield-volcano, Teno, Tenerife (Spain). *Journal of Geophysical Research: Solid Earth* **113**.

Maghdour-Mashhour, R., Hayes, B., Bolhar, R. & Ueckermann, H. (2020). Sill Intrusion into Pyroxenitic Mush and the Development of the Lower–Upper Critical Zone Boundary of the Bushveld Complex: Implications for the Origin of Stratiform Anorthosites and Chromitites in Layered Intrusions. *Journal of petrology* **62**.

Marsh, B. (2004). A magmatic mush column rosetta stone: the McMurdo Dry Valleys of Antarctica. *Eos, Transactions American Geophysical Union* **85**, 497-502.

Martí, J. (2019). Las Cañadas caldera, Tenerife, Canary Islands: A review, or the end of a long volcanological controversy. *Earth-Science Reviews* **196**, 102889.

Martí, J. & Gudmundsson, A. (2000). The Las Cañadas caldera (Tenerife, Canary Islands): an overlapping collapse caldera generated by magma-chamber migration. *Journal of Volcanology and Geothermal Research* **103**, 161-173.

Martí, J., Hurlimann, M., Ablay, G. J. & Gudmundsson, A. (1997). Vertical and lateral collapses on Tenerife (Canary Islands) and other volcanic ocean islands. *Geology* **25**, 879-882.

Martí, J., Mitjavila, J. & Araña, V. (1994). Stratigraphy, structure and geochronology of the Las Cañadas caldera (Tenerife, Canary Islands). *Geological Magazine* **131**, 715-727.

Martí, J., Zafrilla, S., Andújar, J., Jiménez-Mejías, M., Scaillet, B., Pedrazzi, D., Doronzo, D. & Scaillet, S. (2020). Controls of magma chamber zonation on eruption dynamics and deposits stratigraphy: The case of El Palomar fallout succession (Tenerife, Canary Islands). *Journal of Volcanology and Geothermal Research*, 106908.

Masotta, M., Mollo, S., Freda, C., Gaeta, M. & Moore, G. (2013). Clinopyroxene–liquid thermometers and barometers specific to alkaline differentiated magmas. *Contributions to Mineralogy and Petrology* **166**, 1545-1561.

Melekhova, E., Blundy, J., Martin, R., Arculus, R. & Pichavant, M. (2017). Petrological and experimental evidence for differentiation of water-rich magmas beneath St. Kitts, Lesser Antilles. *Contributions to Mineralogy and Petrology* **172**, 98.

Morimoto, N. (1988). Nomenclature of pyroxenes. *Mineralogy and Petrology* **39**, 55-76.

Muñoz, M. & Sagredo, J. (1974). Clinopyroxenes as geobarometric indicators in mafic and ultramafic rocks from Canary Islands. *Contributions to Mineralogy and Petrology* **44**, 139-147.

Mutch, E. J., Maclennan, J., Holland, T. J. & Buisman, I. (2019a). Millennial storage of near-Moho magma. *Science* **365**, 260-264.

Mutch, E. J., Maclennan, J., Shorttle, O., Edmonds, M. & Rudge, J. F. (2019b). Rapid transcrustal magma movement under Iceland. *Nature Geoscience*, 1.

Namur, O., Abily, B., Boudreau, A. E., Blanchette, F., Bush, J. W., Ceuleneer, G., Charlier, B., Donaldson, C. H., Duchesne, J.-C. & Higgins, M. D. (2015). Igneous layering in basaltic magma chambers. *Layered intrusions*: Springer, 75-152.

Neave, D. A., Buisman, I. & Maclennan, J. (2017). Continuous mush disaggregation during the long-lasting Laki fissure eruption, Iceland. *American Mineralogist* **102**, 2007-2021.

Neave, D. A. & Putirka, K. D. (2017). A new clinopyroxene-liquid barometer, and implications for magma storage pressures under Icelandic rift zones. *American Mineralogist* **102**, 777-794.

Neumann, E.-R., Sørensen, V., Simonsen, S. & Johnsen, K. (2000). Gabbroic xenoliths from La Palma, Tenerife and Lanzarote, Canary Islands: evidence for reactions between mafic alkaline Canary Islands melts and old oceanic crust. *Journal of Volcanology and Geothermal Research* **103**, 313-342.

Neumann, E.-R., Wulff-Pedersen, E., Pearson, N. & Spencer, E. (2002). Mantle xenoliths from Tenerife (Canary Islands): evidence for reactions between mantle peridotites and silicic carbonatite melts inducing Ca metasomatism. *Journal of petrology* **43**, 825-857.

Neumann, E.-R., Wulff-Pedersen, E., Simonsen, S., Pearson, N., Martí, J. & Mitjavila, J. (1999). Evidence for fractional crystallization of periodically refilled magma chambers in Tenerife, Canary Islands. *Journal of petrology* **40**, 1089-1123.

Olin, P. H. (2007). Magma dynamics of the phonolitic Diego Hernández Formation, Tenerife, Canary Islands. (published Ph.D dissertation): Washington State University, 430.

Olin, P. H. & Wolff, J. A. (2010). Rare earth and high field strength element partitioning between iron-rich clinopyroxenes and felsic liquids. *Contributions to Mineralogy and Petrology* **160**, 761-775.

Olin, P. H. & Wolff, J. A. (2012). Partitioning of rare earth and high field strength elements between titanite and phonolitic liquid. *Lithos* **128**, 46-54.

Passmore, E., Maclennan, J., Fitton, G. & Thordarson, T. (2012). Mush Disaggregation in Basaltic Magma Chambers: Evidence from the ad 1783 Laki Eruption. *Journal of petrology* **53**, 2593-2623.

Piña-Varas, P., Ledo, J., Queralt, P., Marcuello, A. & Perez, N. (2018). On the detectability of Teide volcano magma chambers (Tenerife, Canary Islands) with magnetotelluric data. *Earth, Planets and Space* **70**, 14.

Pittari, A., Cas, R. A. F., Wolff, J. A., Nichols, H. J., Larson, P. & Martí, J. (2008). The use of lithic clast distributions in pyroclastic deposits to understand pre-and syn-caldera collapse processes: a case study of the Abrigo Ignimbrite, Tenerife, Canary Islands. *Developments in Volcanology* **10**, 97-142.

Putirka, K., Johnson, M., Kinzler, R., Longhi, J. & Walker, D. (1996). Thermobarometry of mafic igneous rocks based on clinopyroxene-liquid equilibria, 0–30 kbar. *Contributions to Mineralogy and Petrology* **123**, 92-108.

Putirka, K. D. (2008). Thermometers and barometers for volcanic systems. *Reviews in mineralogy and geochemistry* **69**, 61-120.

Schleicher, J. M. & Bergantz, G. W. (2017). The Mechanics and Temporal Evolution of an Open-system Magmatic Intrusion into a Crystal-rich Magma. *Journal of petrology* **58**, 1059-1072.

Scott, P. (1976). Crystallization trends of pyroxenes from the alkaline volcanic rocks of Tenerife, Canary Islands. *Mineralogical Magazine* **40**, 805-816.

Simonsen, S., Neumann, E.-R. & Seim, K. (2000). Sr–Nd–Pb isotope and trace-element geochemistry evidence for a young HIMU source and assimilation at Tenerife (Canary Island). *Journal of Volcanology and Geothermal Research* **103**, 299-312.

Sliwinski, J., Bachmann, O., Ellis, B. S., Dávila-Harris, P., Nelson, B. K. & Dufek, J. (2015). Eruption of shallow crystal cumulates during explosive phonolitic eruptions on Tenerife, Canary Islands. *Journal of petrology* **56**, 2173-2194.

Smith, N. J. & Kokelaar, B. P. (2013). Proximal record of the 273 ka Poris caldera-forming eruption, Las Cañadas, Tenerife. *Bulletin of Volcanology* **75**, 1-21.

Solano, J., Jackson, M., Sparks, R., Blundy, J. & Annen, C. (2012). Melt segregation in deep crustal hot zones: a mechanism for chemical differentiation, crustal assimilation and the formation of evolved magmas. *Journal of petrology* **53**, 1999-2026.

Sparks, R., Annen, C., Blundy, J., Cashman, K., Rust, A. & Jackson, M. (2019). Formation and dynamics of magma reservoirs. *Philosophical Transactions of the Royal Society A* **377**, 20180019.

Sparks, R. S. J., Huppert, H. E., Kerr, R., McKenzie, D. & Tait, S. R. (1985). Postcumulus processes in layered intrusions. *Geological Magazine* **122**, 555-568.

Spiegelman, M. & Kelemen, P. B. (2003). Extreme chemical variability as a consequence of channelized melt transport. *Geochemistry, Geophysics, Geosystems* **4**.

Stock, M., Geist, D., Neave, D., Gleeson, M., Bernard, B., Howard, K., Buisman, I. & Maclennan, J. (2020). Cryptic evolved melts beneath monotonous basaltic shield volcanoes in the Galápagos Archipelago.

Stock, M. J., Taylor, R. N. & Gernon, T. M. (2012). Triggering of major eruptions recorded by actively forming cumulates. *Scientific Reports* **2**, 731.

Taddeucci, J., Cimarelli, C., Alatorre-Ibarguenguoitia, M. A., Delgado-Granados, H., Andronico, D., Del Bello, E., Scarlato, P. & Di Stefano, F. (2022). Features of broken crystals reveal the fracturing and healing of basaltic magmas during explosive volcanic eruptions. Copernicus Meetings.

Taylor, R. N., Davila-Harris, P., Branney, M. J., Farley, E. R., Gernon, T. M. & Palmer, M. R. (2020). Dynamics of a chemically pulsing mantle plume. *Earth and Planetary Science Letters* **537**, 116182.

Taylor, S. R. & McLennan, S. M. (1985). The continental crust: its composition and evolution.

Thirlwall, M. (1997). Pb isotopic and elemental evidence for OIB derivation from young HIMU mantle. *Chemical Geology* **139**, 51-74.

Thirlwall, M., Singer, B. & Marriner, G. (2000). 39Ar–40Ar ages and geochemistry of the basaltic shield stage of Tenerife, Canary Islands, Spain. *Journal of Volcanology and Geothermal Research* **103**, 247-297.

Triebold, S., Kronz, A. & Wörner, G. (2006). Anorthite-calibrated backscattered electron profiles, trace elements, and growth textures in feldspars from the Teide–Pico Viejo volcanic complex (Tenerife). *Journal of Volcanology and Geothermal Research* **154**, 117-130.

Troll, V. R., Mattsson, T., Upton, B. G., Emeleus, C. H., Donaldson, C. H., Meyer, R., Weis, F., Dahrén, B. & Heimdal, T. H. (2020). Fault-Controlled Magma Ascent Recorded in the Central Series of the Rum Layered Intrusion, NW Scotland. *Journal of petrology* **61**, egaa093.

Vinkler, A. P., Cashman, K., Giordano, G. & Groppelli, G. (2012). Evolution of the mafic Villa Senni caldera-forming eruption at Colli Albani volcano, Italy, indicated by textural analysis of juvenile fragments. *Journal of Volcanology and Geothermal Research* **235**, 37-54.

Wager, L., Brown, G. & Wadsworth, W. (1960). Types of igneous cumulates. *Journal of petrology* **1**, 73-85.

Walker, G. (1981). Plinian eruptions and their products. *Bulletin Volcanologique* **44**, 223.

Wiesmaier, S., Troll, V. R., Wolff, J. A. & Carracedo, J. C. (2013). Open-system processes in the differentiation of mafic magma in the Teide–Pico Viejo succession, Tenerife. *Journal of the Geological Society* **170**, 557-570.

Wolff, J., Grandy, J. & Larson, P. (2000). Interaction of mantle-derived magma with island crust? Trace element and oxygen isotope data from the Diego Hernandez Formation, Las Cañadas, Tenerife. *Journal of Volcanology and Geothermal Research* **103**, 343-366.

Wolff, J. & Storey, M. (1983). The volatile component of some pumice-forming alkaline magmas from the Azores and Canary Islands. *Contributions to Mineralogy and Petrology* **82**, 66-74.

Wolff, J. A. (1985). Zonation, mixing and eruption of silica-undersaturated alkaline magma: a case study from Tenerife, Canary Islands. *Geological Magazine* **122**, 623-640.

Wolff, J. A. (1987). Crystallisation of nepheline syenite in a subvolcanic magma system: Tenerife, Canary Islands. *Lithos* **20**, 207-223.

Wolff, J. A., Ellis, B., Ramos, F. C., Starkel, W. A., Boroughs, S., Olin, P. H. & Bachmann, O. (2015). Remelting of cumulates as a process for producing chemical zoning in silicic tuffs: A comparison of cool, wet and hot, dry rhyolitic magma systems. *Lithos* **236**, 275-286.

Wolff, J. A., Forni, F., Ellis, B. S. & Szymanowski, D. (2020). Europium and barium enrichments in compositionally zoned felsic tuffs: A smoking gun for the origin of chemical and physical gradients by cumulate melting. *Earth and Planetary Science Letters* **540**, 116251.

Wood, B. J. & Blundy, J. D. (1997). A predictive model for rare earth element partitioning between clinopyroxene and anhydrous silicate melt. *Contributions to Mineralogy and Petrology* **129**, 166-181.

Yagi, K. (1966). The system acmite-diopside and its bearing on the stability relations of natural pyroxenes of the acmite-hedenbergite-diopside series. *American Mineralogist: Journal of Earth and Planetary Materials* **51**, 976-1000.

Yanagida, Y., Nakamura, M., Yasuda, A., Kuritani, T., Nakagawa, M. & Yoshida, T. (2018). Differentiation of a hydrous arc magma recorded in melt inclusions in deep crustal cumulate xenoliths from Ichinomegata Maar, NE Japan. *Geochemistry, Geophysics, Geosystems* **19**, 838-864.

FIGURE CAPTIONS

Fig. 1. (A) The position of Tenerife within the Canary Island chain. **(B)** Map of the southeastern slopes of Tenerife, termed the Bandas del Sur region, maps modified after Stock *et al.* (2012). Sampling localities from this study are marked by white circles (sample geolocations are provided in Supplementary Data). **(C)** Stratigraphic scheme for the phonolitic pyroclastic Members in the Diego Hernández Formation between 0.37–0.18 Ma, after Edgar *et al.* (2007). Graphic log of the Fasnia member **(D)** is from the Las Cañadas caldera wall **(D)**, labelled TR010. A distal log from locality TR008 **(E)** is northwest of the town of Poris de Abona, note

there is difference in scale between the two logs. Units in the Fasnia member are according to the stratigraphic scheme from Edgar *et al.* (2017). Sampling positions of plutonic nodules analysed in this study within the Ravelo ignimbrite are marked in arrows in caldera wall **(D)** and the coastal log **(E)**. Abbreviations used in stratigraphic column annotations are given in the legend (e.g., mLT = massive lapilli tuff).

Fig. 2. Field photos from the lithic breccia facies in Ravelo unit, part of the Fasnia Member. **(A)** Phonolite megablock in the Ravelo ignimbrite, caldera wall locality (TR010). **(B)** Section of the Ravelo unit from the caldera wall log (Fig. 1D). (C) Section of the lithic breccia from locality TR008, with a reduction in clast size range and angularity in the Bandas del Sur region. (D) Locality TR020, coarser lithic breccia layer annotated with the position of the plutonic nodules in the unit. Gas escape structure highlighted by a vertical distribution of denser clasts in the lapilli tuff facies (E) insert, photo of a melt bearing plutonic nodule. (F) Nodule in the Ravelo unit, with grey and vesicular, quenched melt seen depressed relative to upstanding clinopyroxene crystals, note lack of a melt coating on the nodule.

Fig. 3. Petrological and geochemical overview of juvenile nodules from the Fasnia Member. **(A)** Modal mineralogies ranked with increasing proportion of mafic minerals down the stacked bar chart. Modal abundances have been determined from point counting, see methods. Mafic minerals include: ol, cpx, opq, hbl and bt. Felsic minerals are grouped: pl, ap, kfs, foid (abbreviations defined in Table 1 caption). Nodules are separated into three groups; (1) Ultramafic nodules, (2) gabbroic nodules, (3) felsic nodules, marked to the left of the stack. Mineral proportions are normalised to 100%. **(B)** Proportion of interstitial melt recorded in each nodule. **(C)** REE ratios of the interstitial melt, where n represents chondrite-normalised samples using factors from Evensen *et al.* (1978). **(D)** Mg# of interstitial melts separated by nodule group, ultramafic (green circles), the gabbroic group is subdivided into hornblende-bearing nodules (yellow circles) and gabbroic (grey circles), to distinguish between nodules

with and without amphibole in the assemblage and lastly felsic nodules (pink circles) (n=51). Mg# of clinopyroxene crystals, larger green squares plot the average clinopyroxene composition per sample, the smaller green symbols denoting all measured crystal compositions (n= 556).

Fig. 4. Photomicrographs displaying a range of textures from the Fasnia nodules **(A)** SEM image of sample TR008-20, highlighting the structure in the microcrystalline groundmass. **(B)** Magnified SEM image of microlites growth textures on the face of plagioclase crystal. **(C)** XPL image of fabrics showing a preferential orientation of tabular grains, and a relatively uniform grain size distribution (range 0.25-2.4 mm) of hornblende, plagioclase and clinopyroxene (sample L1_54). **(D)** XPL image of a sample with three interpreted layers marked by white dashes, based on melt abundance, any grain shape orientation and mineral abundance, (sample L1_44). Layer 1: coarser grained crystals (higher abundance of plagioclase and groundmass), with a random grain shape orientation and a higher abundance of microcrystalline groundmass. Layer 2: hornblende dominated, grain-supported fabric. Layer 3: dominated by plagioclase and minor clinopyroxene, a crude fabric defined by the orientation of tabular plagioclase **(E)** Edited PPL images of a modally graded layer (sample TR008_12), defined by changes in mineralogy: a layer with higher proportions of feldspathoids (highlighted in blue) and minor plagioclase (grey), and plagioclase-rich, groundmass-poor layers. **(F)** XPL image showing grain size and groundmass layered gabbro sample (TEM_02B). **(G)** XPL image showing euhedral and un-deformed clinopyroxene grains with smaller, anhedral glomerocrysts, alongside examples of sector zoning, a microcrystalline groundmass-rich gabbroic sample (TR007_01). **(H)** PPL image of a groundmass-supported feldspathoid syenite (TEM05_03) with black arrows indicating sieve textures developed in K-feldspars.

Fig. 5. Optical petrographic features of the ultramafic nodules. **(A)** XPL image showing sector zoned cumulus clinopyroxene grains (highlighted by white arrows; wehrlite sample L2_57). **(B)** PPL image of a clinopyroxene containing poikilitic olivine inclusions in PPL (wehrlite sample L2_57). **(C)** PPL image of biotite clinopyroxenite sample TR010_04, biotite crystals (0.1-1.2 mm) and clusters of biotite are labelled. **(D)** XPL image of a clinopyroxenite sample (L1_14) with discrete melt pathway, grain size coarsening away from pathway and clinopyroxene linear inclusion trails, with examples marked by white arrows and a close up shown in insert **(E)**.

Fig. 6. Photomicrographs showing variable plagioclase morphology and dissolution textures in Fasnia nodules. **(A)** XPL image showing plagioclase crystals that are melt-invaded, with dissolved cores (sample L1-3). **(B)** XPL image showing incipient dissolution of a plagioclase core with interconnected melt producing a sieve texture (sample L1-15). **(C)** XPL image showing plagioclase crystals with equilibrium, undissolved grain boundaries and un-zoned clinopyroxenes containing opaques (sample L1-37). **(D)** XPL image showing single crystals of clinopyroxene replacing the centre of the sieve textured cores in plagioclase with irregular grain boundaries (sample L1_56). **(E)** XPL image showing a sieve texture in clinopyroxene (melt infiltrated), highlighted by a white arrow, and apatite circled in white (sample TR008_12). **(F-G)** PPL images of green clinopyroxene cores (marked by white arrows) with apatite (circled) and opaque inclusions (**F:** sample L1_58, **G:** sample TEM_01A).

Fig. 7. Summary of clinopyroxene chemistry. **(A)** Pyroxene classification ternary diagram Morimoto (1988) for Ca-Mg-Fe pyroxenes with the black field highlighting the position of the Fasnia Ca-Mg clinopyroxenes (Type-1, 2 & 3). **(B)** Expanded field of view of the ternary diagram separating out the clinopyroxene cumulate types: Type-1 Al-rich titanaugite (purple; photo **D**), Type-2 Fe-rich titanaugite cores (dark green; photo **E** outlined core), Type-3 Al-poor

titanaugite (light green; photo **F**). **(C)** Ternary diagram including Na clinopyroxenes from Morimoto (1988) (Q >80 representing Ca-Mg-Fe pyroxenes) with black square representing pyroxene compositions measured from syenite clast (aegirine). **(D-F)** Types of clinopyroxene observed in PPL in Fasnia cumulates. **(G)** Aegirine pyroxenes from syenite clast, showing examples of sector zoning.

Fig. 8. Clinopyroxene compositions from the Fasnia nodules, classified by compositional/optical type and cumulate group (see legend, top right). Clinopyroxene data from Fasnia pumice from Olin (2007) are shown as grey squares (n=136). Data are shown as atoms per formula unit (a.p.f.u), assuming six oxygens. kernel density estimation (KDE) curves show the probability distribution of clinopyroxene compositions (**A**: Al KDE in grey; **C**: Mg KDE in black), highlights the high-Al and low-Al populations from our three nodule groups (n=556). **(E)** Mg# distribution by nodule group and clinopyroxene type with corresponding KDE curves for Type-1 cpx (separated into peaks; ultramafic, hbl-bearing and gabbroic groups), Type-2 cpx cores (all nodule groups), Type-3 cpx (felsic nodules) and Fasnia pumice clinopyroxene Olin (2007). Error bars show 2σ analytical uncertainties where this is greater than the size of a data point.

Fig. 9. Chemical compositions of all erupted products from the Fasnia Member. This includes; interstitial melts (this study), Fasnia bulk-rock pumice (this study; blue triangles with black outline and Olin (2007); blue triangles or labelled as blue field in major element plots A-D), Fasnia glasses (Olin, 2007) and syenite blocks (this study and Olin (2007)), see legend in C. Note that syenite clasts from this study are from the Fasnia Member. For these syenite clasts, these come from either the Fasnia or the Abrigo Member (DHF I) from Olin (2007) and Wolff *et al.* (2000). The grey field shows a compilation of all bulk-rock data from Tenerife (from the GEOROC database). **(A)** TAS plot after (Le Bas *et al.*, 1986a). **(B)** Bivariate plot showing

MgO versus TiO_2, with an insert magnifying the low-Mg samples. **(C)** Bivariate plot showing MgO versus Al_2O_3. **(D)** MgO versus CaO. Grey open circles in **(B-D)** plot the bulk rock compositions calculated using a mass balance of mineral and melt proportions with each samples corresponding modal mineral proportions (Fig. 3), average mineral composition and bulk rock nodule composition is given in the Supplementary data. **(E)** REE $[La/Sm]_n$ and $[Dy/Yb]_n$, as examples of the relationship between LREE/MREE and MREE/HREE. **(F)** Zr versus Eu/Eu*, a measure of the behaviour of Eu relative to other REE, is expressed as Eu/Eu*, a geometric mean ($=[Eu]n/([Sm]n.[Gd]n)^{0.5}$), calculated following Taylor and McLennan (1985). Eu anomalies above 1.0 referred to as positive and below 1.0 are negative. Error bars show 2σ analytical uncertainties where this is greater than the size of a data symbol.

Fig. 10. Summary of interstitial melt compositions separated by nodule group. **(A)** Major element compositions of Fasnia interstitial melts on a total alkali-silica (TAS) plot, separated by our three host nodule groups, with the gabbroic group (2) subdivided into hornblende-bearing and gabbroic (see legend). Bars above the TAS plot show the SiO_2 variability between the groups of interstitial melts (n=37). **(B)** Examples of rare-earth element ratios plotting Fasnia interstitial melts, [La/Sm]n versus [Dy/Yb]n, separated by the host nodule group's lithology. Bars above **(B)** show the range of [La/Sm]n and [Dy/Yb]n ratios between the groups, where n represents chondrite-normalised samples using factors from Evensen *et al.* (1978). Error bars show 2σ analytical uncertainties where this is greater than the size of a data symbol.

Fig. 11. (A-C) Chondrite-normalised REE patterns for interstitial liquids and pumices from the Fasnia Member. **(A)** Ultramafic nodules, **(B)** hornblende-bearing and gabbroic cumulates, **(C)** felsic nodules, and **(D)** pumice samples (this study), with syenite bulk rock data from Olin (2007) shown in the light grey field. The average REE profile for all measured interstitial melts

is shown in each plot as a black dashed line. Chondrite normalisation factors are from Evensen *et al.* (1978). **(E-H)** REE of pyroxene separates plotted as their calculated equilibrium liquids, separated by pyroxene type and nodule group. Annotated with image of pyroxene type. To invert clinopyroxene composition into its predicted liquid composition, calculated KD's for Na-rich pyroxene (Type-2, 3 and aegirine), were calculated using methods from Beard *et al.* (2019) and for Al-rich titanaugite (Type-1 cpx) KD's were calculated using the Wood and Blundy (1997) method, KD values and parameters are given in the Supplementary material.

Fig. 12. (A-C) Mineral – melt mixing plots with interstitial melt compositions separated by cumulate group, with the gabbroic group (2) subdivided into hornblende-bearing and gabbroic (see legend). Average Type-1 clinopyroxene (this study), plagioclase (TEM-05) and K-feldspar (L1-25) compositions plotted as white squares, Zr content of K-feldspar calculated assuming equilibrium with average phonolite (average of 491 phonolites from Diego Hernández Formation) with Zr = 1075 ppm and a K-feldspar/phonolite kd of 0.056 (Jeffery & Gertisser, 2018). Mixing lines are shown between plagioclase, average basanite (blue diamond), and average Diego Hernández phonolite (blue triangle), tick lines marking 20% intervals. Compositions used for average basanite lavas < 1 Ma, <48% SiO_2 data from Wolff *et al.* (2000) and Carracedo *et al*. (2007). The grey field shows a general Tenerife trend. **(A)** Eu/Eu* versus Al_2O_3. **(B)** Zr versus Al_2O_3. **(C)** K_2O versus Al_2O_3. **(D-E)** Plots of interstitial melt chemistry separated by plagioclase textures in the nodules, no plagioclase, non-dissolved plagioclase and sieve textured plagioclase (dissolved).

Fig. 13: Schematic representation of the volcanic system at the time of the Diego Hernández Formation alongside depth estimates of the sub-volcanic structures from previous studies. Caldera outline is adapted from Cas *et al.* (2022). Mafic cumulate body(s) have been identified

from geophysical studies at depths of 5–14 km below central Tenerife (Ablay & Kearey, 2000, Araña *et al.*, 2000)† and geobarometry (Neumann *et al.*, 1999)§. Shallow syenitic plutons (shaded blue) were emplaced at depths of 4–7 km below the Las Canadas summit, multiple times over the depositional history of the Ucana, Guajara and Diego Hernández Formations (post 1.6 Ma) (Ablay, 1998, Ablay *et al.*, 1995, Bryan *et al.*, 2000, Wolff *et al.*, 2000, Wolff, 1987). Andújar *et al.* (2008) estimating the phonolite at the roof of the Abrigo magma reservoir was at 4–5 km below the surface. Left panel represents a period where the melts are ascending through the system and contributing to a phonolite reservoir composition, right panel is depicting the fragmentation of the conduit, wall rock, syenite plutons and deeper mafic-felsic mush reservoir that constitute the lithic clasts entrained in the Ravelo ignimbrite during the caldera collapse event (Edgar *et al.*, 2017).

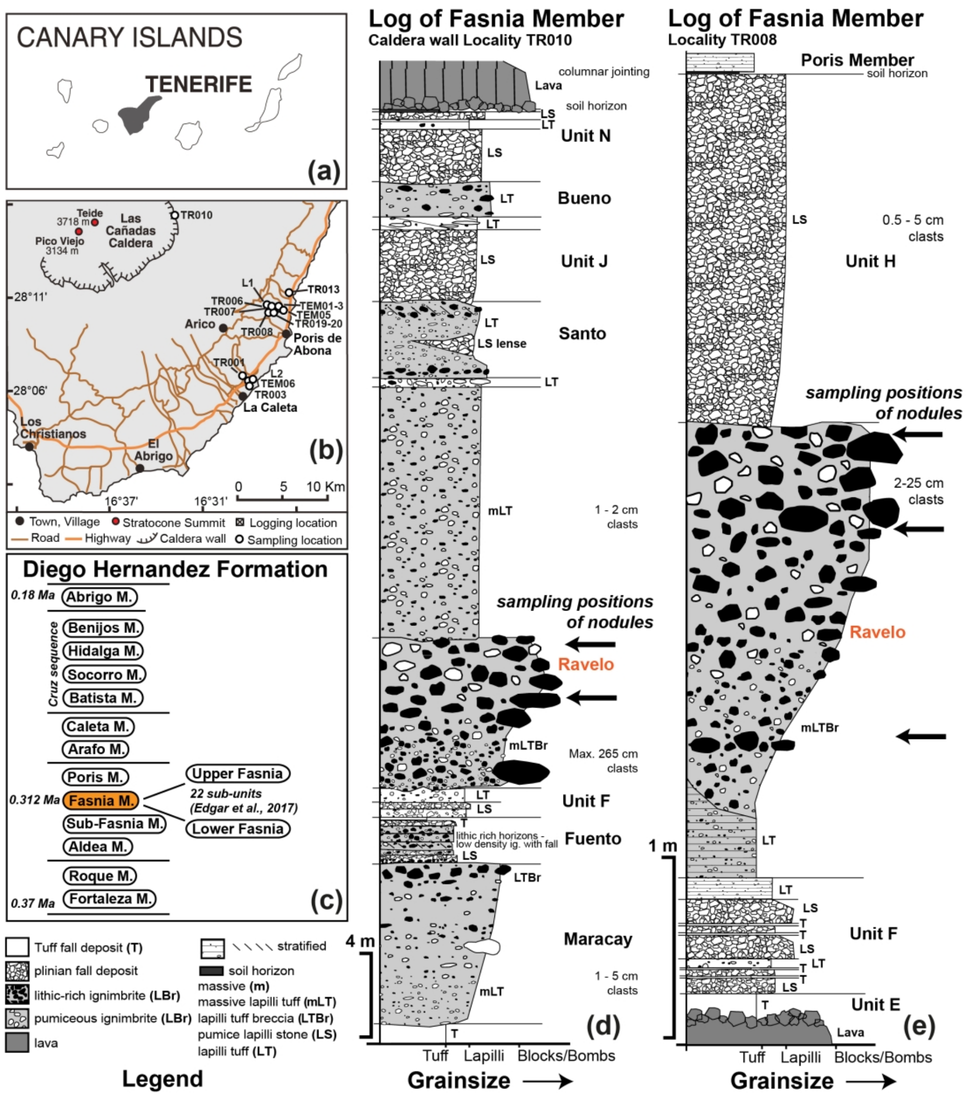

Fig. 1. (A) The position of Tenerife within the Canary Island chain. (B) Map of the southeastern slopes of Tenerife, termed the Bandas del Sur region, maps modified after Stock et al. (2012). Sampling localities from this study are marked by white circles (sample geolocations are provided in Supplementary Data). (C) Stratigraphic scheme for the phonolitic pyroclastic Members in the Diego Hernández Formation between 0.37–0.18 Ma, after Edgar et al. (2007). Graphic log of the Fasnia member (D) is from the Las Cañadas caldera wall (D), labelled TR010. A distal log from locality TR008 (E) is northwest of the town of Poris de Abona, note there is difference in scale between the two logs. Units in the Fasnia member are according to the stratigraphic scheme from (Edgar et al., 2017). Sampling positions of plutonic nodules analysed in this study within the Ravelo ignimbrite are marked in arrows in caldera wall (D) and the coastal log (E). Abbreviations used in stratigraphic column annotations are given in the legend (e.g., mLT = massive lapilli tuff).

204x227mm (300 x 300 DPI)

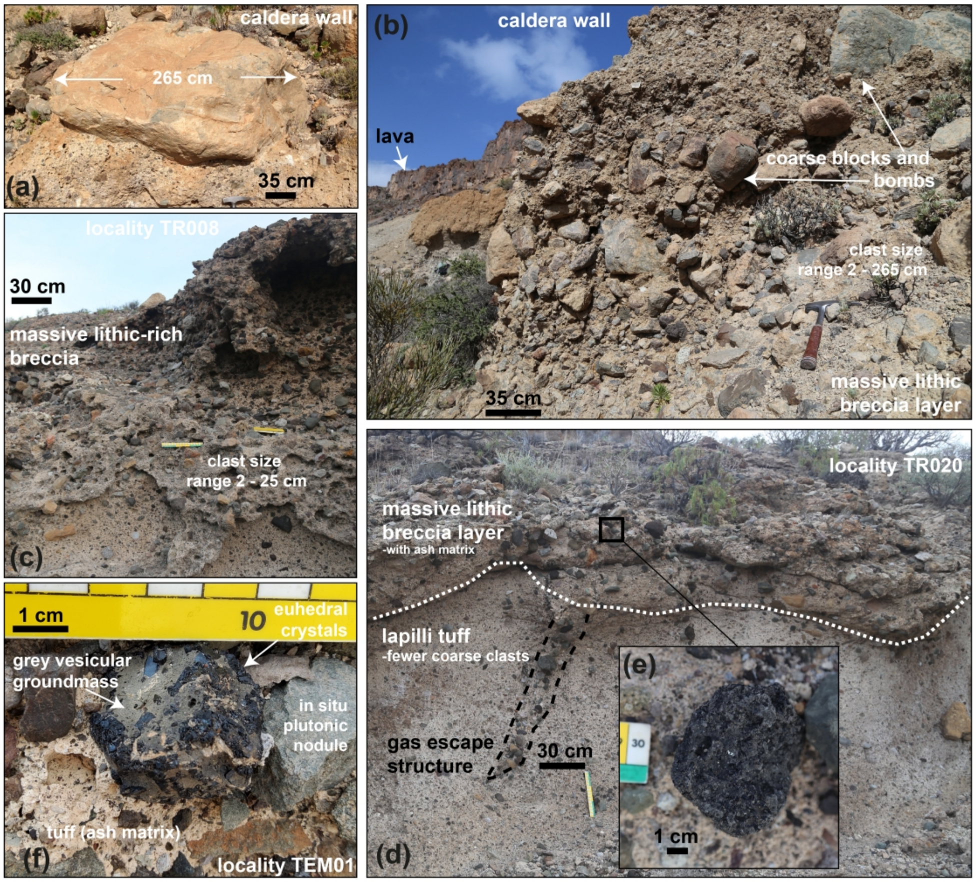

Fig. 2. Field photos from the lithic breccia facies in Ravelo unit, part of the Fasnia Member. (A) Phonolite megablock in the Ravelo ignimbrite, caldera wall locality (TR010). (B) Section of the Ravelo unit from the caldera wall log (Fig. 1D). (C) Section of the lithic breccia from locality TR008, with a reduction in clast size range and angularity in the Bandas del Sur region. (D) Locality TR020, coarser lithic breccia layer annotated with the position of the plutonic nodules in the unit. Gas escape structure highlighted by a vertical distribution of denser clasts in the lapilli tuff facies (E) insert, photo of a melt bearing plutonic nodule. (F) Nodule in the Ravelo unit, with grey and vesicular, quenched melt seen depressed relative to upstanding clinopyroxene crystals, note lack of a melt coating on the nodule.

319x287mm (300 x 300 DPI)

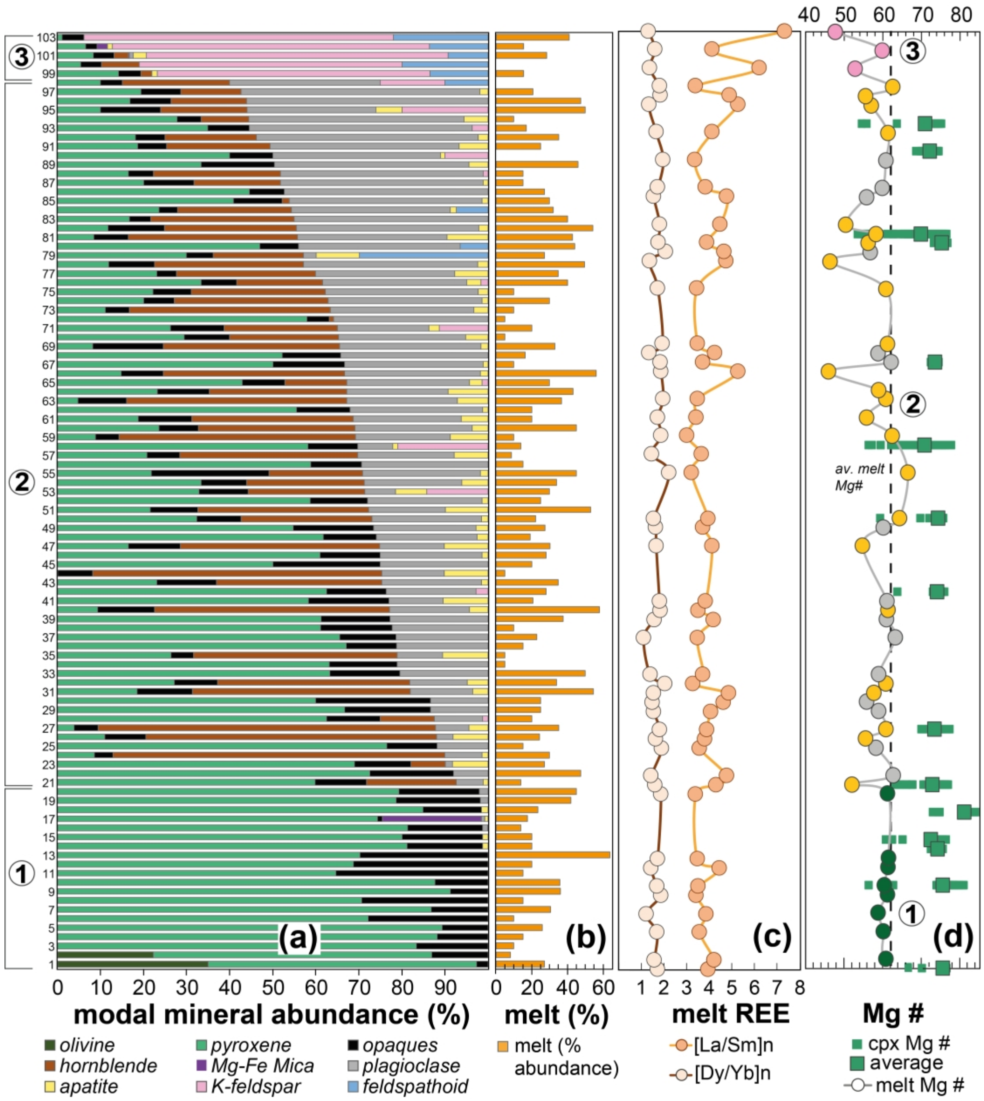

Fig. 3. Petrological and geochemical overview of juvenile nodules from the Fasnia Member. (A) Modal mineralogies, are ranked with increasing proportion of mafic minerals down the stacked bar chart. Modal abundances have been determined from point counting, see methods. Mafic minerals include: ol, cpx, opq, hbl and bt. Felsic minerals are grouped: pl, ap, kfs, foid (abbreviations defined in Table 1 caption). Nodules are separated into three groups; (1) Ultramafic nodules, (2) gabbroic nodules, (3) felsic nodules, marked to the left of the stack. Mineral proportions are normalised to 100%. (B) Proportion of interstitial melt recorded in each nodule. (C) REE ratios of the interstitial melt, where n represents chondrite-normalised samples using factors from Evensen et al. (1978). (D) Mg# of interstitial melts separated by nodule group, ultramafic (green circles), the gabbroic group is subdivided into hornblende-bearing nodules (yellow circles) and gabbroic (grey circles), to distinguish between nodules with and without amphibole in the assemblage and lastly felsic nodules (pink circles) (n=51). Mg# of clinopyroxene crystals, larger green squares plot the average clinopyroxene composition per sample, the smaller green symbols denoting all measured crystal compositions (n=556).

352x398mm (300 x 300 DPI)

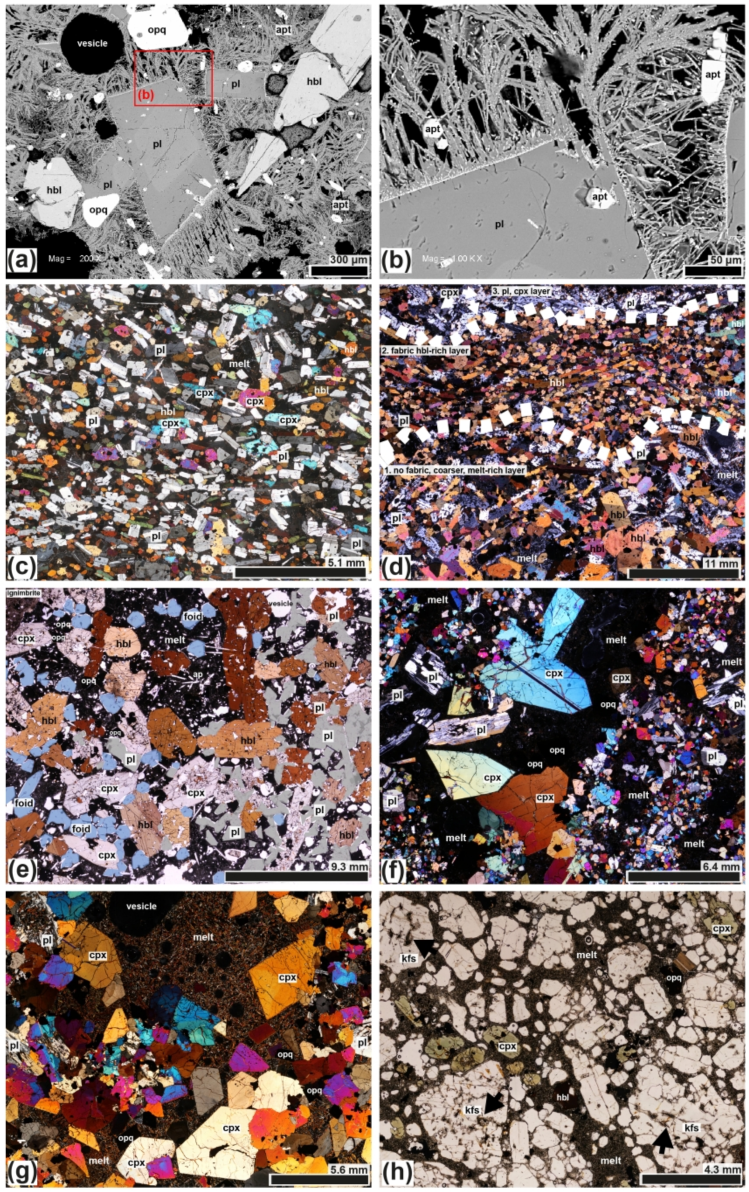

Fig. 4. Photomicrographs displaying a range of textures from the Fasnia nodules (A) SEM image of sample TR008-20, highlighting the structure in the microcrystalline groundmass. (B) Magnified SEM image of microlites growth textures on the face of plagioclase crystal. (C) XPL image of fabrics showing a preferential orientation of tabular grains, and a relatively uniform grain size distribution (range 0.25-2.4 mm) of hornblende, plagioclase and clinopyroxene (sample L1_54). (D) XPL image of a sample with three interpreted layers marked by white dashes, based on groundmass abundance, any grain shape orientation and mineral abundance, (sample L1_44). Layer 1: coarser grained crystals (higher abundance of plagioclase and melt), with a random grain shape orientation and a higher abundance of melt. Layer 2: hornblende dominated, grain-supported fabric. Layer 3: dominated by plagioclase and minor clinopyroxene, a crude fabric defined by the orientation of tabular plagioclase (E) Edited PPL image of a modally graded layer (sample TR008_12), defined by changes in mineralogy: a layer with higher proportions of feldspathoids (highlighted in blue) and minor plagioclase (grey), and plagioclase-rich, melt-poor layers. (F) XPL image showing grain size and melt layered gabbro sample (TEM_02B). (G) XPL image showing euhedral and un-deformed clinopyroxene grains with smaller, anhedral glomerocrysts, alongside examples of sector zoning, a

melt-rich gabbroic sample (TR007_01). (H) PPL image of a melt-supported feldspathoid syenite (TEM05_03) with black arrows indicating sieve textures developed in K-feldspars.

205x324mm (300 x 300 DPI)

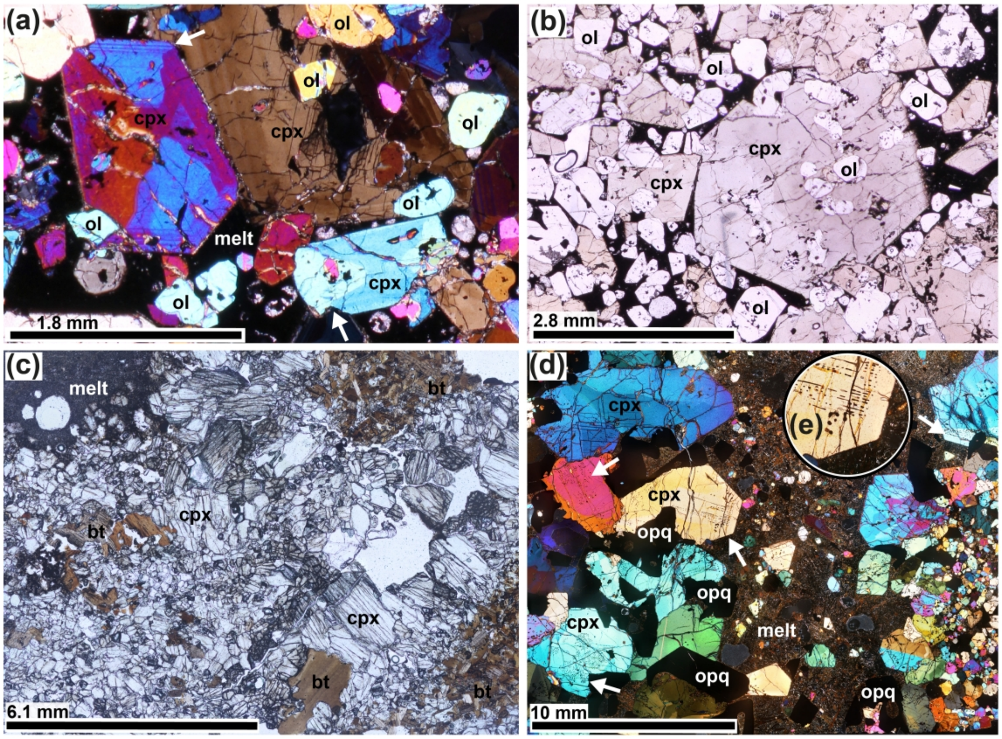

Fig. 5. Optical petrographic features of the ultramafic nodules. (A) XPL image showing sector zoned cumulus clinopyroxene grains (highlighted by white arrows; wehrlite sample L2_57). (B) PPL image of a clinopyroxene containing poikilitic olivine inclusions in PPL (wehrlite sample L2_57). (C) PPL image of biotite clinopyroxenite sample TR010_04, biotite crystals (0.1-1.2 mm) and clusters of biotite are labelled. (D) XPL image of a clinopyroxenite sample (L1_14) with discrete melt pathway, grain size coarsening away from pathway and clinopyroxene linear inclusion trails, with examples marked by white arrows and a close up shown in insert (E).

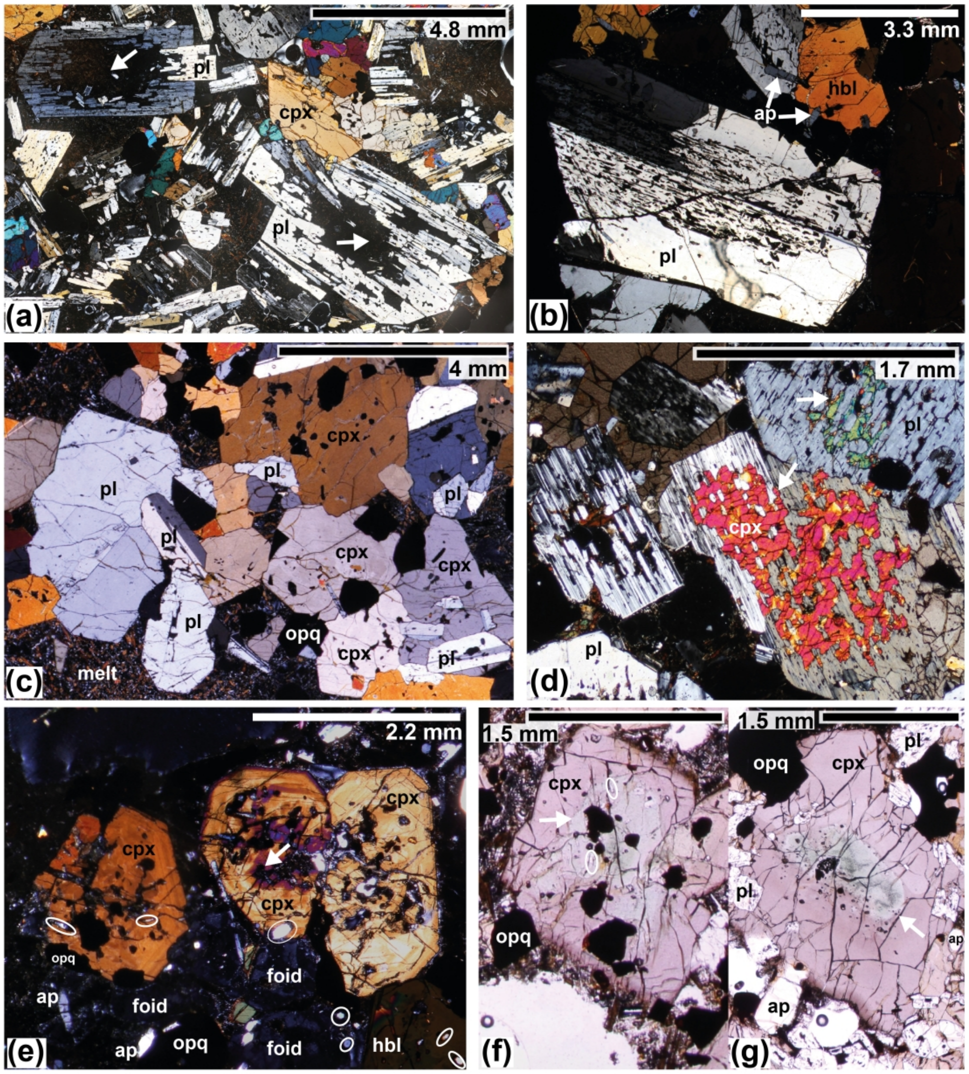

Fig. 6. Photomicrographs showing variable plagioclase morphology and dissolution textures in Fasnia nodules. (A) XPL image showing plagioclase crystals that are melt-invaded, with dissolved cores (sample L1-3). (B) XPL image showing incipient dissolution of a plagioclase core with interconnected melt producing a sieve texture (sample L1-15). (C) XPL image showing plagioclase crystals with equilibrium, undissolved grain boundaries and un-zoned clinopyroxenes containing opaques (sample L1-37). (D) XPL image showing single crystals of clinopyroxene replacing the centre of the sieve textured cores in plagioclase with irregular grain boundaries (sample L1_56). (E) XPL image showing a sieve texture in clinopyroxene (melt infiltrated), highlighted by a white arrow, and apatite circled in white (sample TR008_12). (F-G) PPL images of green clinopyroxene cores (marked by white arrows) with apatite (circled) and opaque inclusions (F: sample L1_58, G: sample TEM_01A).

362x395mm (300 x 300 DPI)

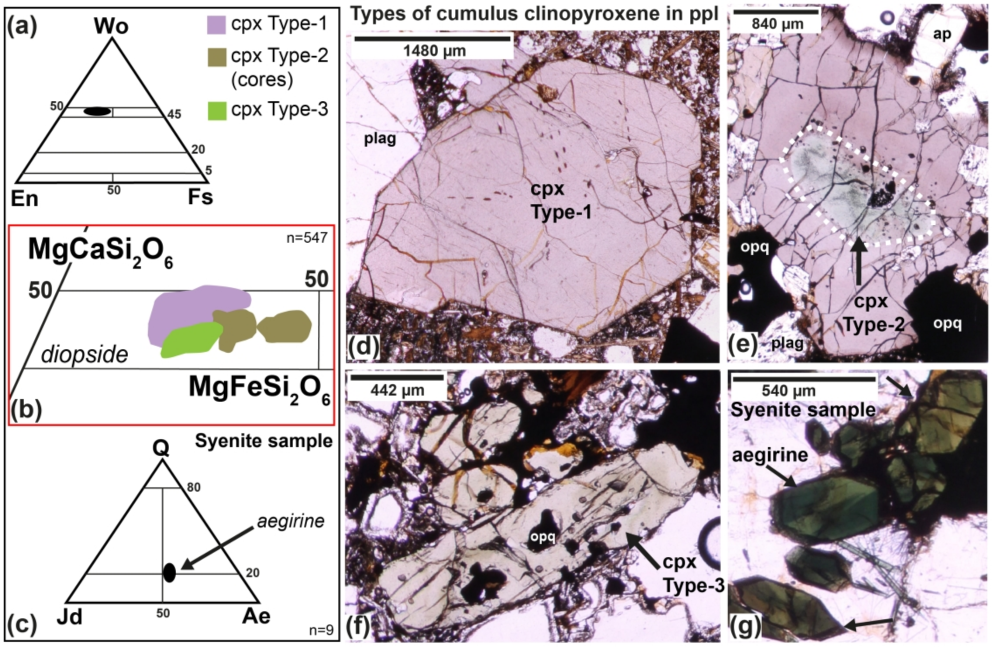

Fig. 7. Summary of clinopyroxene chemistry. (A) Pyroxene classification ternary diagram (Morimoto, 1988) for Ca-Mg-Fe pyroxenes with the black field highlighting the position of the Fasnia Ca-Mg clinopyroxenes (type-1, 2 & 3). (B) Expanded field of view of the ternary diagram separating out the clinopyroxene cumulate types: Type-1 Al-rich titanaugite (purple; photo D), Type-2 Fe-rich titanaugite cores (dark green; photo E outlined core), Type-3 Al-poor titanaugite (light green; photo F). (C) Ternary diagram including Na clinopyroxenes from (Morimoto, 1988), (Q >80 representing Ca-Mg-Fe pyroxenes) with black square representing pyroxene compositions measured from syenite clast (aegirine- aegirine-augite). (D-F) Types of clinopyroxene observed in PPL in Fasnia cumulates. (G) Aegirine pyroxenes from syenite clast, showing examples of sector zoning.

288x188mm (300 x 300 DPI)

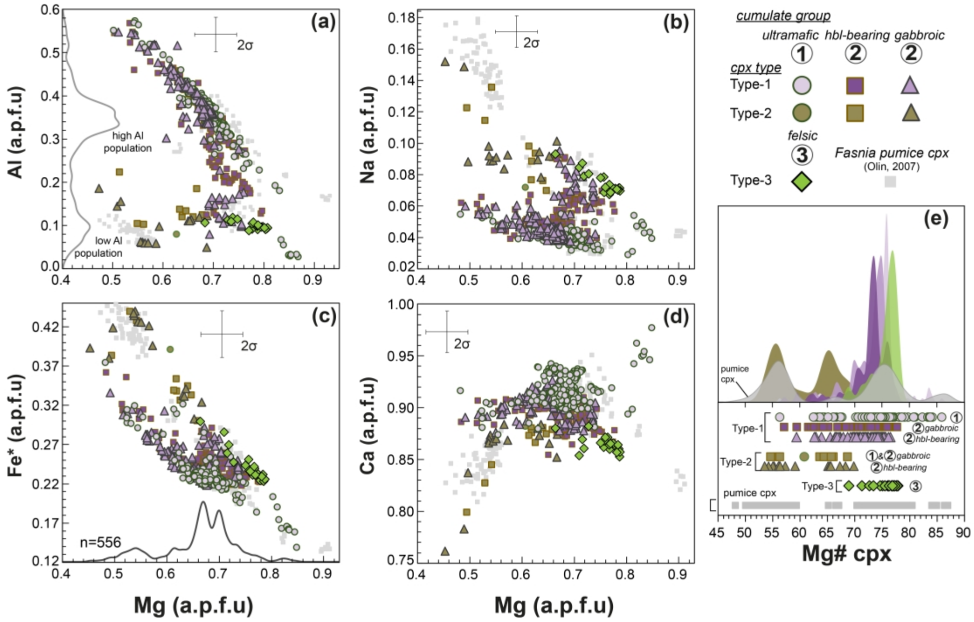

Fig. 8. Clinopyroxene compositions from the Fasnia nodules, classified by compositional/optical type and cumulate group (see legend, top right). Clinopyroxene data from Fasnia pumice from Olin (2007) are shown as grey squares (n=136). Data are shown as atoms per formula unit (a.p.f.u), assuming six oxygens. kernel density estimation (KDE) curves show the probability distribution of our nodule clinopyroxene compositions (A: Al KDE in grey; C: Mg KDE in black), highlights the high-Al and low-Al populations from our three nodule groups. (n=556). (E) Mg# distribution by nodule group and clinopyroxene type with corresponding KDE curves for Type-1 cpx (separated into peaks; ultramafic, hbl-bearing and gabbroic groups), Type-2 cpx cores (all nodule groups), Type-3 cpx (felsic nodules) and Fasnia pumice clinopyroxene (Olin, 2007). Error bars show 2σ analytical uncertainties where this is greater than the size of a data point.

406x255mm (300 x 300 DPI)

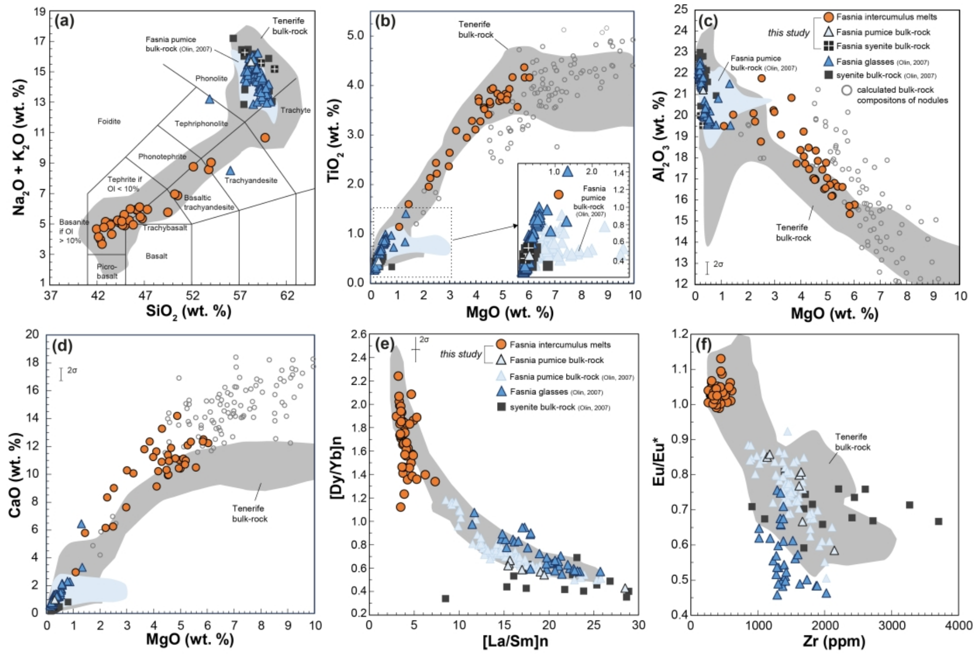

Fig. 9. Chemical compositions of all erupted products from the Fasnia Member. This includes; intercumulus melts (this study), Fasnia bulk-rock pumice (this study; blue triangles with black outline and Olin (2007); blue triangles or labelled as blue field in major element plots A-D), Fasnia glasses (Olin, 2007) and syenite blocks (this study and Olin (2007)), see legend in C. Note that syenite clasts from this study are from the Fasnia Member. measuring major elements (Supplementary Data) and trace element data is from Olin (2007). For these syenite clasts, these come from either the Fasnia or the Abrigo Member (DHF I) from Olin (2007) and Wolff et al., (2000). The grey field shows a compilation of all bulk-rock data from Tenerife (from the GEOROC database). (A) TAS plot after Le Bas (1986). (B) Bivariate plot showing MgO versus TiO_2, with an insert magnifying the low-Mg samples. (C) Bivariate plot showing MgO versus Al_2O_3. (D) MgO versus CaO. Grey open circles in (B-D) plot the bulk rock compositions calculated using a mass balance of mineral and melt proportions with each samples corresponding modal mineral proportions (Fig. 3), average mineral composition and bulk rock nodule composition is given in the Supplementary data. (E) REE [La/Sm]n and [Dy/Yb]n, as examples of the relationship between LREE/MREE and MREE/HREE. (F) Zr versus Eu/Eu*, a measure of the behaviour of Eu relative to other REE, is expressed as Eu/Eu*, a geometric mean (=[Eu]n/([Sm]n.[Gd]n)$^{0.5}$), calculated following (Taylor & McLennan, 1985). Eu anomalies above 1.0 referred to as positive and below 1.0 are negative. Error bars show 2σ analytical uncertainties where this is greater than the size of a data symbol.

681x458mm (150 x 150 DPI)

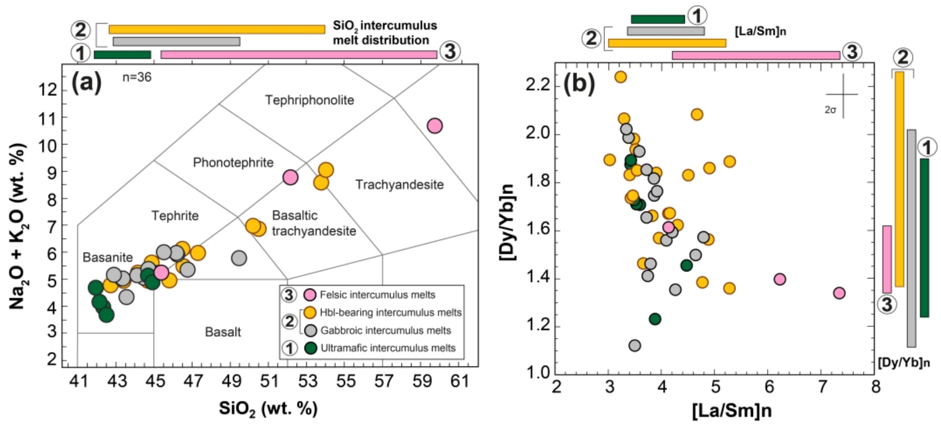

Fig. 10. Summary of interstitial melt compositions separated by nodule group. (A) Major element compositions of Fasnia interstitial melts on a total alkali-silica (TAS) plot, separated by our three host nodule groups, with the gabbroic group (2) subdivided into hornblende-bearing and gabbroic (see legend). Bars above the TAS plot show the SiO_2 variability between the groups of interstitial melts (n=37). (B) Examples of rare-earth element ratios plotting Fasnia interstitial melts, [La/Sm]n versus [Dy/Yb]n, separated by the host nodule group's lithology. Bars above (B) show the range of [La/Sm]n and [Dy/Yb]n ratios between the groups, where n represents chondrite-normalised samples using factors from Evensen et al. (1978). Error bars show 2σ analytical uncertainties where this is greater than the size of a data symbol.

522x218mm (300 x 300 DPI)

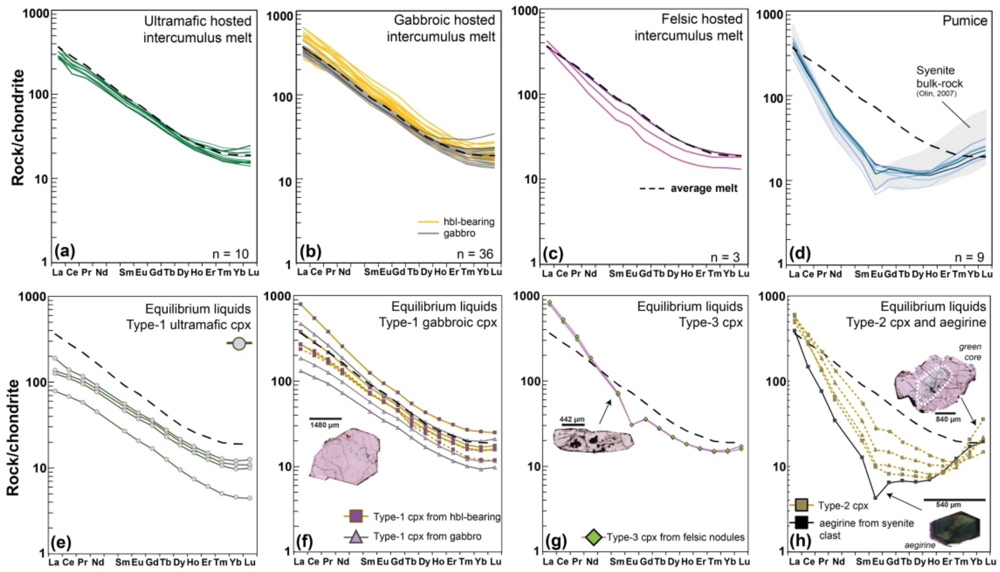

Fig. 11. (A-C) Chondrite-normalised REE patterns for interstitial liquids and pumices from the Fasnia Member. (A) Ultramafic nodules, (B) hornblende-bearing and gabbroic cumulates, (C) felsic nodules, and (D) pumice samples (this study), with syenite bulk rock data from Olin (2007) shown in the light grey field. The average REE profile for all measured interstitial melts is shown in each plot as a black dashed line. Chondrite normalisation factors are from Evensen et al. (1978). (E-H) REE of pyroxene separates plotted as their calculated equilibrium liquids, separated by pyroxene type and nodule group. Annotated with image of pyroxene type. To invert clinopyroxene composition into its predicted liquid composition, calculated KD's for Na-rich pyroxene (Type-2, 3 and aegirine), were calculated using methods from Beard et al. (2019) and for Al-rich titanaugite (Type-1 cpx) KD's were calculated using the Wood and Blundy (1997) method, KD values and parameters are given in the Supplementary material.

483x276mm (300 x 300 DPI)

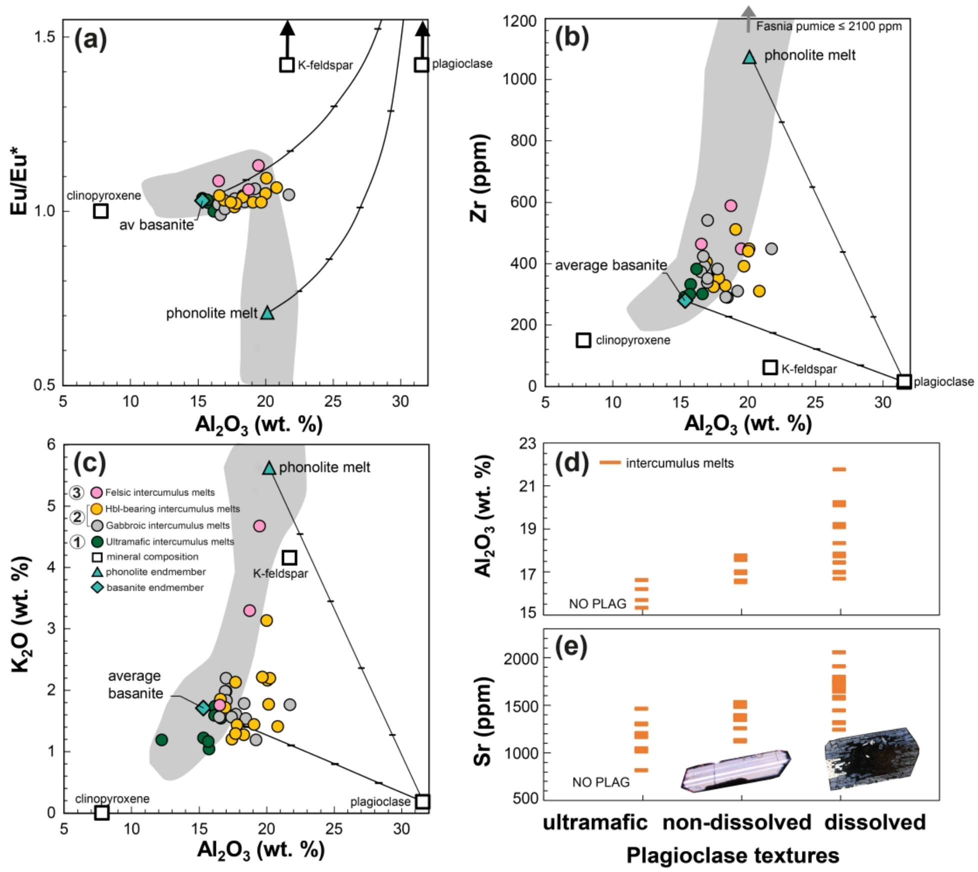

Fig. 12. (A-C) Mineral – melt mixing plots with interstitial melt compositions separated by cumulate group, with the gabbroic group (2) subdivided into hornblende-bearing and gabbroic (see legend). Average Type-1 clinopyroxene (this study), plagioclase (TEM-05) and K-feldspar (L1-25) compositions plotted as white squares, Zr content of K-feldspar calculated assuming equilibrium with average phonolite (average of 491 phonolites from Diego Hernández Formation) with Zr = 1075 ppm and a K-feldspar/phonolite kd of 0.056 (Jeffery & Gertisser, 2018). Mixing lines are shown between plagioclase, average basanite (blue diamond), and average Diego Hernández phonolite (blue triangle), tick lines marking 20% intervals. Compositions used for average basanite lavas < 1 Ma, <48% SiO_2 data from Wolff et al. (2000) and Carracedo et al. (2007). The grey field shows a general Tenerife trend. (A) Eu/Eu* versus Al_2O_3. (B) Zr versus Al_2O_3. (C) K_2O versus Al_2O_3. (D-E) Plots of interstitial melt chemistry separated by plagioclase textures in the nodules, no plagioclase, non-dissolved plagioclase and sieve textured plagioclase (dissolved).

407x355mm (300 x 300 DPI)

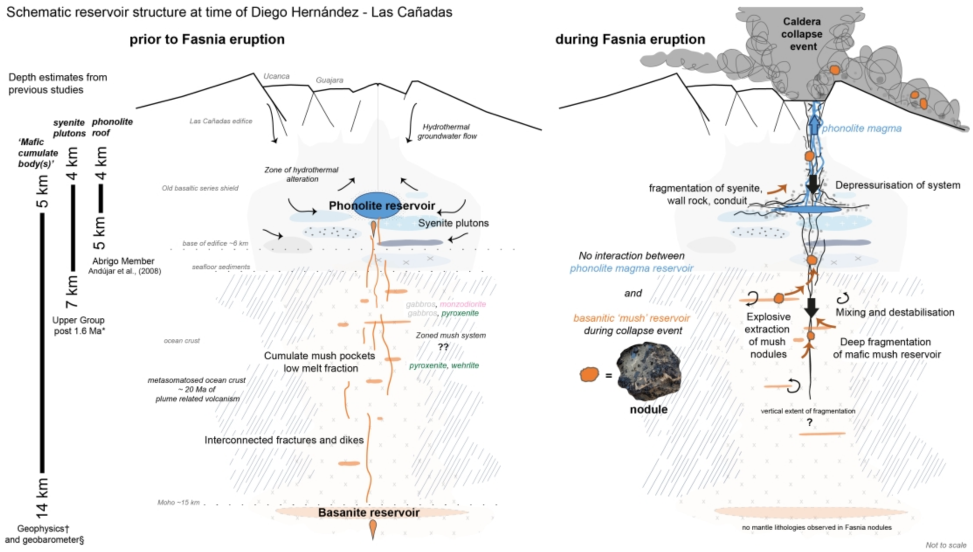

Fig. 13: Schematic representation of the volcanic system at the time of the Diego Hernández Formation alongside depth estimates of the sub-volcanic structures from previous studies. Caldera outline is adapted from Cas et al. (2022). Mafic cumulate body(s) have been identified from geophysical studies at depths of 5–14 km below central Tenerife (Ablay & Kearey, 2000, Araña et al., 2000)† and geobarometry (Neumann et al., 1999)§. Shallow syenitic plutons (shaded blue) were emplaced at depths of 4–7 km below the Las Canadas summit, multiple times over the depositional history of the Ucana, Guajara and Diego Hernández Formations (post 1.6 Ma) (Ablay, 1998, Ablay et al., 1995, Bryan et al., 2000, Wolff et al., 2000, Wolff, 1987). With Andújar et al. (2008) estimating the phonolite at the roof of the Abrigo magma reservoir was at 4–5 km below the surface. Left panel represents a period where the melts are ascending through the system and contributing to a phonolite reservoir composition, right panel is depicting the fragmentation of the conduit, wall rock, syenite plutons and deeper mafic-felsic mush reservoir that constitute the lithic clasts entrained in the Ravelo ignimbrite during the caldera collapse event (Edgar et al., 2017).

305x173mm (300 x 300 DPI)

Table 1. Summary of lithological, mineralogical, grain size and melt abundance data for 103 juvenile cumulate samples used in this study.

Group	Cumulate sample type	No. of samples	Mineral assemblage (**major** ± minor)	Major mineral abundance vol% range **(average)**	Grain size range (mm)	Melt abundance range **(average)**	Cumulate density **(g/cm^3)****
1	*Wehrlite*	2	**ol, cpx** ± opq	ol, 21 – 26 **(23)** cpx, 45 – 60 **(52)**	0.1 – 5.0	8 – 27 **(17.6)**	3.3 - 3.4
1	*Clino-pyroxenite*	18	**cpx**, **opq** ± pl	cpx, 25 – 75 **(59)** opq, 1 – 30 **(14.2)**	0.5 – 12.0	10 – 64 **(25.5)**	3.4 – 3.5
2	*Gabbro*	30	**cpx, pl**, opq ± ap ± kfs ± hbl + foid ± rt	cpx, 18 – 60 **(43)** pl, 4 – 43 **(21)**	0.5 – 20.0	0 – 50 **(23.0)**	3.2 – 3.3
2	*Hornblende-bearing**	47	**hbl, cpx, pl,** opq ± ap ± kfs ± foid	hbl, 6 – 64 **(45)** pl, 1 – 45 **(15)** cpx, 0 – 52 **(21)**	0.5 – 32.0	5 – 58 **(26.1)**	3.0 – 3.3
3	*Feldspathoid syenite, monzodiorite*	6	**kfs, foid, pl** ± cpx ± hbl ± bt ± opq ± ap	kfs, 15 – 62 **(47)** foid, 7 – 20 **(12)** pl, 0 – 35 **(7)**	0.2 – 5.5	0 – 41 **(16.7)**	2.7 – 2.8

Classification and nomenclature of plutonic rocks from Streckeisen (1974). Major mineral phases (>5 vol%) are in bold and minor mineral phase (<5 vol%) in normal text, with abbreviations: olivine (ol), clinopyroxene (cpx), hornblende (hbl), plagioclase (pl), k-feldspar (kfs), feldspathoid (foid), opaque (opq), apatite (ap), biotite (bt), rutile (rt). *hornblende-bearing cumulates include pyroxene hornblende gabbros, pyroxene hornblendite, hornblende pyroxenite and hornblende gabbro cumulate lithologies. **cumulate densities are calculated using a weighted average of the density and vol% of the minerals present in each cumulate lithology. Melt densities are calculated from the average melt abundance and average major element composition (presented in Supplementary material), following the procedure used in Bottinga and Weill (1970).

Table 2: Average major element compositions for Fasnia clinopyroxenes

Cumulate group	Ultramafic	Ultramafic	Gabbroic	Gabbroic	Gabbroic	Gabbroic	Felsic	Syenite
Sample/s	L1_89 & L2_57B	4 samples*	L1_37	TEM_01 A_cpx_3	TEM_01 A_cpx_3	L1_59_ cpx_8	L1_94	L1_71
No. of crystals	10	33	5	1	1	1	6	5
Data points	100	124	44	54	8	12	21	9
cpx type	type-1	type-1	type-1	type-1**	type-2	type-2	type-3	aegirine
SiO_2	45.9	44.5	44.7	44.9	50.0	50.9	51.5	52.0
TiO_2	2.89	3.64	3.67	3.55	1.25	0.81	1.02	2.79
Al_2O_3	7.43	8.48	8.38	8.04	3.28	2.16	2.28	1.03
FeO	7.23	7.57	7.28	7.91	10.73	12.64	7.79	23.83
MnO	0.10	0.14	0.13	0.19	0.65	1.2	0.66	0.79
MgO	12.62	11.77	11.9	11.61	10.89	9.59	13.6	2.18
CaO	23.14	22.66	22.64	22.24	21.36	20.87	21.66	4.83
Na_2O	0.44	0.52	0.50	0.62	1.15	1.27	0.97	10.70
Mg#	75.6	73.4	74.4	72.2	64.3	57.4	75.7	13.9
X_{En}	37.9	36.4	36.9	36.2	33.7	30.2	40.6	11.2
X_{Wo}	39.9	50.4	50.4	49.9	48.0	47.4	46.4	17.6
X_{Fs}	12.1	13.2	12.7	13.9	18.71	22.4	13.0	71.2

A summary of clinopyroxene data from EMPA and grouped by clinopyroxene and sample type (ultramafic, gabbroic, felsic and syenite block). *clinopyroxenes grouped from clinopyroxenite nodules and include samples TR007_02, TEM_02A, TR008_06G & TR003_03. A complete clinopyroxene dataset is provided in the Supplementary material. **measured crystal is a type-1 mantle and rim surrounding a type-2 green core (pictured in Fig. 7E).